

# Chapter 10

## Ultralow-Frequency Raman Spectroscopy of Two-dimensional Materials



Miao-Ling Lin and Ping-Heng Tan

**Abstract** In two-dimensional materials (2DMs), atoms within one layer (in-plane) are joined by covalent bonds, whereas van der Waals (vdW) interactions keep the layers together. Raman spectroscopy is a powerful tool for measuring the lattice vibrational modes in 2DMs, including the intralayer and interlayer vibrations, and has shown great potential for the characterizations of the layer number, interlayer coupling and layer-stacking configurations in 2DMs via the ultralow-frequency (ULF) interlayer vibrational modes. This chapter begins with an introduction of how the monolayer 2DMs stack to assemble a large family of two-dimensional systems (Section 10.1), which are likely to exhibit modified interlayer coupling and thus various ULF mode behaviours. In sequence, Section 10.2 provides a detailed description of the physical origins of the interlayer vibrations and the linear chain model (LCM) to depict their layer-number dependent frequencies. Subsequently, two popular Raman setups are introduced to perform the ULF modes measurements (Section 10.3). Then, we provide a review of the ULF Raman spectroscopy of various types of 2DMs, including: (1) layer-number dependent (Section 10.4.1) and (2) stacking-order dependent (Section 10.4.2) ULF Raman spectroscopy in isotropic 2DMs; (3) ULF Raman spectroscopy in anisotropic 2DMs (Section 10.4.3); and (4) ULF Raman modes in twisted 2DMs (Section 10.4.4) and heterostructures (Section 10.4.5).

---

The original version of this chapter was revised. A correction to this chapter is available at [https://doi.org/10.1007/978-981-13-1828-3\\_12](https://doi.org/10.1007/978-981-13-1828-3_12)

M.-L. Lin

State Key Laboratory of Superlattices and Microstructures, Institute of Semiconductors, Chinese Academy of Sciences, Beijing, China

College of Materials Science and Opto-Electronic Technology, University of Chinese Academy of Science, Beijing, China

P.-H. Tan (✉)

State Key Laboratory of Superlattices and Microstructures, Institute of Semiconductors, Chinese Academy of Sciences, Beijing, China

Center of Materials Science and Opto-Electronics Engineering & CAS Center of Excellence in Topological Quantum Computation, University of Chinese Academy of Sciences, Beijing, China  
e-mail: [phtan@semi.ac.cn](mailto:phtan@semi.ac.cn)

## 10.1 Introduction

Two dimensional (2D) materials can usually be exfoliated from bulk layered materials (LMs), which form strong in-plane chemical bonds, but have weak out-of-plane van der Waals (vdW) interactions [1, 2]. The enormous interest in 2D materials (2DMs) is fuelled by the desire to investigate the unique optoelectronic properties of these ultra-thin flakes. Actually, 2DMs constitute a large family [1, 3–7]. The diverse and novel physical properties of these 2DMs are usually ascribed to their different symmetries and various interlayer coupling [3, 5, 7]. Thus, 2DMs can be classified according to their symmetry [2]. Large advances have been made on the ultrathin 2DMs whose bulk forms belong to  $D_{6h}$  symmetry, such as graphite and TMDs. Recently, much attention has been paid to the 2DMs with low symmetry due to their in-plane anisotropy. 2DMs consist of one or more rigid layers. Each rigid layer can be regarded as one individual *layer* in 2DMs or LMs. The stacking of these layers along the  $c$  axis can form the corresponding multilayer (ML) 2DMs, and  $N$  layer ( $NL$ ) 2DMs contains  $N$  rigid layers in the flakes. The symmetries in ML 2DMs are likely to be reduced because the out-of-plane translational symmetry will break. For example, the  $D_{6h}$  in graphite is reduced to  $D_{3h}$  and  $D_{3d}$  for ML graphenes (MLGs) with odd and even layer numbers (ONLs and ENLs), respectively, whereas it remains  $D_{6h}$  for monolayer graphene (1LG).

The stacking order of the layers in 2DMs can be different, which leads their symmetries as well as the properties to become more diverse. Taking the in-plane isotropic  $\text{MoS}_2$  as a simple example, as shown in Fig. 10.1a, monolayer  $\text{MoS}_2$  belongs to  $D_{3h}$  symmetry, referred to as 1H- $\text{MoS}_2$ . The stacking of 1H- $\text{MoS}_2$  along the  $c$  axis can generate two common polytypes, 2H (H represents hexagonal) and 3R (R represents rhombohedral), as shown in Fig. 10.1b. The obvious difference between 2H and 3R begins from the second layer. The stacking along the  $c$  axis in 3R only undergoes a layer shift, whereas the  $N$ th layer of 2H stacking is rotated by  $180^\circ$  with respect to the  $(N-1)$ th layer. Thus, the 3R-stacking  $\text{MoS}_2$  from the monolayer to bulk preserves noncentrosymmetry. However, in 2H stacking, ENL  $\text{MoS}_2$  possesses an inversion symmetry point, but ONL  $\text{MoS}_2$  is noncentrosymmetric. Furthermore, the metal atoms can also behave in an octahedral coordination in which the spatial inversion symmetry is preserved in the monolayer  $\text{MoS}_2$ , forming the new polytype 1T stacking, as depicted in right panel of Fig. 10.1b. The different symmetries of these three stackings lead to different interlayer couplings and electronic properties [8]. The symmetries and interlayer couplings in polytypic  $\text{MoS}_2$  and other 2DMs can be easily distinguished by ultralow-frequency (ULF) Raman spectroscopy [2, 6, 9–11]. In addition, during the mechanical exfoliation of 2DM flakes, one thin flake with layer number  $n$  (denoted as  $nL$ -2DM,  $n = 1, 2, \dots$ ) may be randomly folded onto another flake with a layer number  $m$  (denoted as  $mL$ -2DM,  $m = 1, 2, \dots$ ) to form a twisted-2DM ( $t(m+n)L$ -2DM). For example, 1LG can be stacked onto another 1LG and 2LG with a twist angle  $\theta_t$  to form a twisted 2LG and 3LG, denoted as  $t(1+1)LG$  and  $t(1+2)LG$ , as shown in Fig. 10.1c, d, respectively. These twisted systems have been achieved in graphene [12–14],

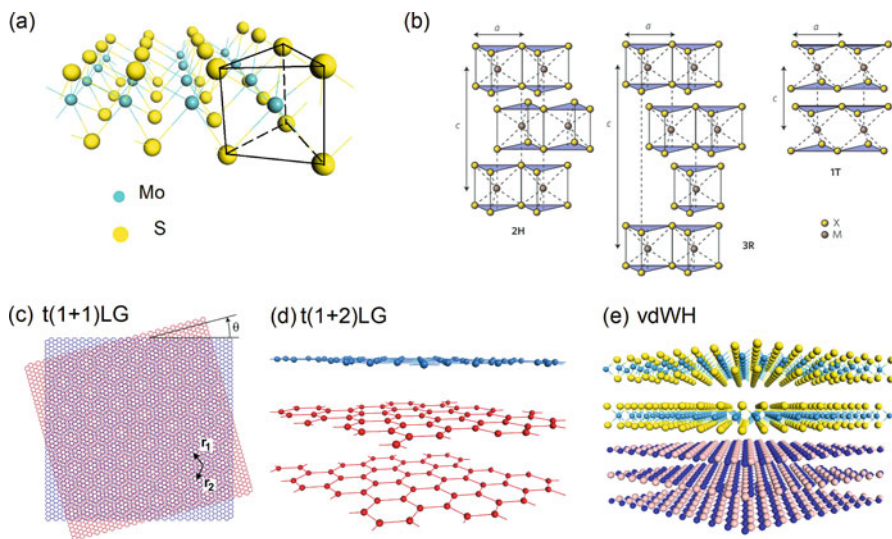


**Fig. 10.1** (a) Schematic diagram of the three-dimensional structure of 1L-MoS<sub>2</sub>. The triangle indicated by black lines display the trigonal prismatic coordination of Mo atoms. (b) Schematic diagrams of the three typical structural polytypes of MX<sub>2</sub>: 2H, 3R and 1T.  $a$  and  $c$  represent the in-plane and out-of-plane lattice constants, respectively. (Reproduced with permission from Ref. [4]). (c) Schematics of a rotationally stacked bilayer graphene with the slant one sitting on the top. The top and bottom layers are rotated with respect to each other by a generic angle  $\theta_t$ , generating a periodic Moiré pattern.  $\mathbf{r}_1$  and  $\mathbf{r}_2$  are the direct vectors defining the supercell. The schematic of (d)  $t(1+2)$ LG with  $\theta_t = 21.8^\circ$  and (e) 2D heterostructures from the side view

MoS<sub>2</sub>, MoSe<sub>2</sub> [15–17] and so on. For a given layer number  $N$ , the choices of  $m$ ,  $n$  and the relative twist angles between two individual constituents leads to another large family of 2DMs with a variety of optical and electronic properties. The recent research frontier has also advanced to investigate hybrid systems of 2DMs. The flat and inert surfaces of these systems enable us to assemble stacks of different 2D heterostructures in a chosen sequence, coupled vertically only by vdW interactions (Fig. 10.1e), which can offer large opportunities for designing the functionalities of these vdW heterostructures (vdWHs). The interfacial interactions between two atomic layers from adjacent constituents of vdWHs can dramatically influence the properties of vdWHs and induce remarkable phenomena that are absent in individual constituents [18–20].

Thus, developing a direct way to detect the interlayer and interfacial coupling in all types of the above 2DMs and related vdWHs is critically needed to investigate their physical and chemical properties. Raman scattering is an important and versatile tool for probing lattice vibrations, including the intralayer and interlayer modes [2, 6, 9–11]. In contrast to the intralayer vibrations, which are driven by the chemical bonds in the plane, interlayer vibrations, i.e., the shear and layer-breathing modes, are determined by the interlayer coupling. It should be noted that the shear

mode is referred to as the  $C$  mode in multilayer graphenes (MLGs) because it provides a direct measurement of the interlayer *Coupling* and was first observed in AB-stacked MLGs [21]. Other notations for the shear modes, such as SM, and for layer-breathing modes, such as the B modes or LBM have been introduced by various research groups [10]. As a general notation for interlayer vibrational modes in layered materials, in this chapter, we denote the shear mode and layer breathing mode as the S and LB modes, [10], respectively. Because the restoring forces of the interlayer modes are weak due to the vdW interactions, the frequencies of these modes are expected to arise in the ULF region. In the following sections, we will provide a broad overview of ULF Raman spectroscopy in 2DMs and related vdWHs.

## 10.2 Physical Origin of Ultralow-Frequency Raman Modes in 2DMs

In ML 2DMs, the relative motions of the atoms in each monolayer result in the so-called intralayer Raman modes, which have high frequencies, whereas the interlayer vibrations in the ULF region are induced by the relative motions of adjacent layers (Fig. 10.2). As referred to in Sect. 10.1, there are two typical interlayer Raman modes, the S and LB modes, which are perpendicular or parallel to their normals, respectively. All of these lattice vibrations at the Brillouin zone (BZ) centre ( $\Gamma$ ) can be expressed by the irreducible representations based on their symmetries, and the number of the vibrational branches ( $3 \times n$ ) depends on the number of atoms ( $n$ ) in the unit cell. For example, there are two atoms in the unit cell of 1LG ( $D_{6h}$ ), so there are six vibrations (three acoustic phonons and three optical phonons), which can be represented by:  $\Gamma = E_{2g} + E_{1u} + B_{2g} + A_{2u}$ . The  $E_{1u}$  and  $A_{2u}$  are assigned to the acoustic phonons, whereas the others correspond to the optical phonons at  $\Gamma$ . Because there is only one layer in 1LG, no interlayer Raman modes are expected. For graphite, all the modes become doublets:  $\Gamma = 2(E_{2g} + E_{1u} + B_{2g} + A_{2u})$ . The interlayer vibrations can be denoted  $E_{2g}$  (for the S mode) and  $B_{2g}$  (for the LB mode) [21]. Due to the different symmetries between ENL graphenes (ENLGs) and ONL graphenes (ONLGs), the vibrations can be represented by  $\Gamma = N E_g + N E_u + N A_{1g} + N A_{2u}$  for ENLGs and  $\Gamma = (N-1)A'_1 + (N+1)A''_2 + (N+1)E' + (N-1)E''$  for ONLGs, respectively. For a NLG, there are  $N-1$  LB modes and  $N-1$  pairs of doubly degenerate S modes. Hence, the interlayer vibrations in NLG can be represented by  $\frac{N}{2}(A_{1g} + E_g) + (\frac{N}{2}-1)(A_{2u} + E_u)$  for ENLG and  $\frac{(N-1)}{2}(E' + E'' + A'_1 + A''_2)$  for ONLG, as shown in Fig. 10.2a, b. For the in-plane isotropic  $N$ -layer 2DMs (denoted as NL-2DMs), each S mode is doubly degenerate and belong to irreducible representation  $E$ , whereas the LB modes belong to irreducible representation  $A$  or  $B$ . Therefore, the S modes are independent on the in-plane polarization, whereas the LB modes exhibit high dependence on the excitation polarization direction, with the result that the LB

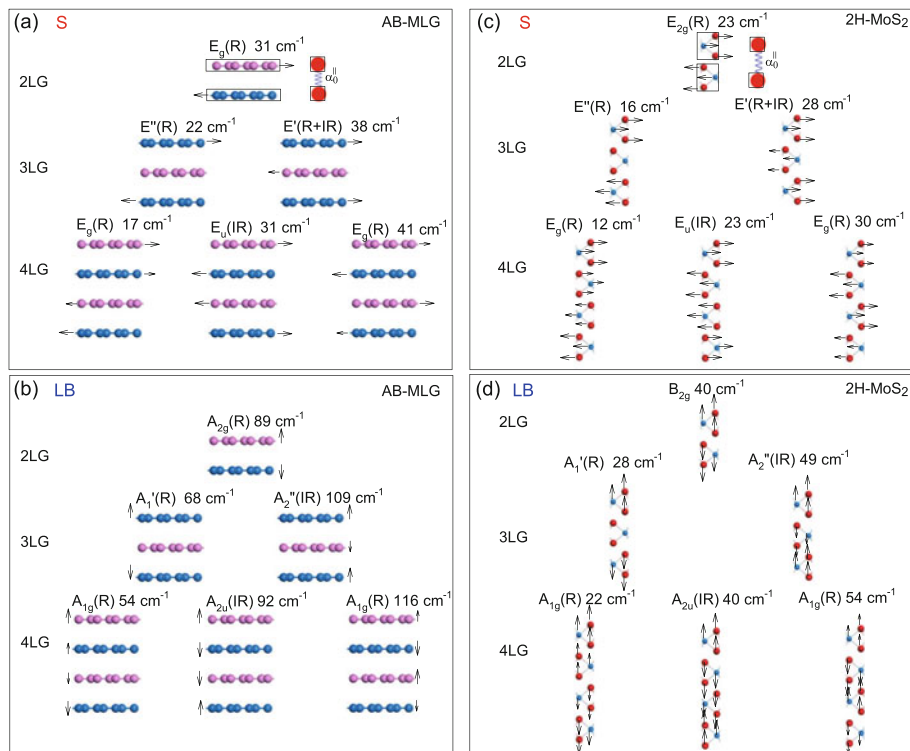


**Fig. 10.2** Symmetry, frequency, Raman activity and normal mode displacements for the S (a) and LB (b) modes in AB-(2-4)LG and the S (c) and LB (d) modes in 2-4L 2H-MoS<sub>2</sub>. R represents Raman active, and IR represents infrared active. The frequencies are calculated from the LCM. The arrows indicate the vibrational directions of the corresponding layers and the length represents the amplitude of the displacement

modes cannot be detected in the cross polarization (HV). This implies that the LB and S modes can be distinguished via the polarized Raman spectroscopy. The assignments of interlayer vibrations in MoS<sub>2</sub> and other TMDs are similar to those in MLGs (Fig. 10.2c, d) due to the semblable symmetries [2, 6]. Moreover, all lattice vibrations in 2DMs, especially the interlayer modes, can be deduced from their symmetries, and those for typical 2DMs are listed in Table 10.1. In general, not all S and LB modes can be observed in Raman spectroscopy because of Raman inactivities or zero Raman intensities in special Raman configurations, as well as the weak electron-phonon interactions.

Here, we present an insight into the frequencies of these interlayer vibrations. For the S and LB modes in 2DMs, the relative displacements between the atoms in each rigid layer can be ignored. Therefore, each rigid layer can be treated as a single ball and only the nearest interlayer coupling is considered, as shown in Fig. 10.2a, c, when we calculate the frequencies of the S and LB modes in 2DMs.

**Table 10.1** Symmetries, irreducible representations of Raman modes at  $\Gamma$  and interlayer vibrations in 1L, ONL and ENL 2DMs and the corresponding bulk LMs. All  $E$  are doubly degenerate

Materials	Thickness	Symmetry	Irreducible representations	Interlayer vibrations
Graphenes	1L	$D_{6h}^1$	$E_{2g}+E_{1u}+B_{2g}+A_{2u}$	–
	ONL	$D_{3h}^1$	$(N-1)A'_1+(N+1)A''_2$ $+(N+1)E'+(N-1)E''$	$\frac{(N-1)}{2}(A'_1+A''_2+E'+E'')$
	ENL	$D_{3d}^3$	$NE_g+NE_u+NA_{1g}+NA_{2u}$	$\frac{N}{2}(E_g+A_{1g})+(\frac{N}{2}-1)(E_u+A_{2u})$
2H-MX <sub>2</sub> (M = Mo, W,	Bulk	$D_{6h}^4$	$2(E_{2g}+E_{1u}+B_{2g}+A_{2u})$	$E_{2g}+B_{2g}$
	1L	$D_{3h}^1$	$A'_1+E''+2(A''_2+E')$	–
X = S, Se, Te)	ONL	$D_{3h}^1$	$\frac{3N-1}{2}(A'_1+E'')$ $+ \frac{3N+1}{2}(A''_2+E')$	$\frac{N-1}{2}(A'_1+E''+A''_2+E')$
	ENL( $N \neq 2$ )	$D_{3d}^3$	$\frac{3N}{2}(A_{1g}+A_{2u}+E_g+E_u)$	$\frac{N}{2}(A_{1g}+E_g)+(\frac{N}{2}-1)(A_{2u}+E_u)$
Bi <sub>2</sub> Se(Te) <sub>3</sub>	bulk	$D_{6h}^4$	$A_{1g}+2A_{2u}+B_{1u}+2B_{2g}$ $+E_{1g}+2E_{1u}+E_{2u}+2E_{2g}$	$E_{2g}+B_{2g}$
	ONL	$D_{3d}^3$	$\frac{5N-1}{2}(A_{1g}+E_g)$ $+ \frac{5N+1}{2}(A_{2u}+E_u)$	$\frac{N-1}{2}(A_{1g}+E_g+A_{2u}+E_u)$
	ENL	$D_{3d}^3$	$\frac{5N}{2}(A_{1g}+E_g+A_{2u}+E_u)$	$\frac{N}{2}(A_{1g}+E_g)+(\frac{N}{2}-1)(A_{2u}+E_u)$
BP	Bulk	$D_{3d}^5$	$2A_{1g}+2E_g+3A_{2u}+3E_u$	–
	ONL	$D_{2h}^7$	$N(2A_g+B_{1g}+2B_{2g}+B_{3g}$ $+A_u+2B_{1u}+B_{2u}+2B_{3u})$	$\frac{N-1}{2}(A_g+B_{2g}+B_{3g})$ $+B_{1u}+B_{2u}+B_{3u}$
	ENL	$D_{2h}^{11}$	$N(2A_g+B_{1g}+2B_{2g}+B_{3g}$ $+A_u+2B_{1u}+B_{2u}+2B_{3u})$	$\frac{N}{2}(A_g+B_{2g}+B_{3g})$ $+ (\frac{N}{2}-1)(B_{1u}+B_{2u}+B_{3u})$
$\beta$ -GaS(Se)	Bulk	$D_{2h}^{18}$	$2A_g+B_{1g}+2B_{2g}+B_{3g}$ $+A_u+2B_{1u}+B_{2u}+2B_{3u}$	$A_g+B_{1u}+B_{3u}$
	Bulk	$D_{6h}^4$	$2(E_{2g}+E_{1u}+B_{2g}+A_{2u})$ $+A_{1g}+B_{1u}+E_{1g}+E_{2u}$	$E_{2g}+B_{2g}$
	Bulk	$D_{3h}^1$	$4(A'_1+E''+A''_2+E')$	$A'_1+E'$
GeS(Se), SnS(Se)	Bulk	$D_{2h}^{16}$	$4A_{1g}+4B_{1u}+2B_{1g}+2A_u$ $+4B_{2g}+4B_{3u}+2B_{3g}+2B_{2u}$	$A_g+B_{2g}+B_{3g}$
CuS(>55k)	Bulk	$D_{6h}^4$	$2A_{1g}+4A_{2u}+4B_{2g}+2B_{1u}$ $+2E_{1g}+4E_{1u}+4E_{2g}+2E_{2u}$	$E_{2g}+B_{2g}$
CuS(<55k)	Bulk	$D_{2h}^{17}$	$6A_g+4B_{1g}+2B_{2g}+6B_{3g}$ $+2A_u+5B_{1u}+5B_{2u}+3B_{3u}$	$A_g+B_{2g}+B_{3g}$
2H-SnS(Se) <sub>2</sub>	Bulk	$D_{3d}^3$	$A_{1g}+2A_{2u}+E_g+2E_u$	$A_{1g}+E_g$
4H-SnS(Se) <sub>2</sub>	Bulk	$C_{6v}^4$	$3(A_1+B_1+E_1+E_2)$	$A_1+E_2$
6Ha-SnS(Se) <sub>2</sub>	Bulk	$C_{3v}$	$9(A_1+E)$	$A_1+E$
6Hb-SnS(Se) <sub>2</sub>	Bulk	$D_{3d}^3$	$4A_{1g}+5A_{2u}+4E_g+5E_u$	$A_{1g}+E_g$
GaTe	Bulk	$C_{2h}^3$	$6(2A_g+B_g+A_u+2B_u)$	$2A_g+B_g$
ReS(Se) <sub>2</sub>	Bulk	$C_i$	$18(A''+A')$	$2A''+A'$

This model is known as the linear chain model (LCM) [21]. Assuming the interlayer interactions per unit area between two adjacent rigid layers as  $\alpha_0^{\parallel}$  and  $\alpha_0^{\perp}$  for the S and LB modes, respectively, the frequencies and atomic displacements of the S and LB modes in  $NL$ -2DMs can be calculated by solving linear homogenous equations as follows [13, 21]:

$$\omega_i^2 \mathbf{u}_i = \frac{1}{2\pi^2 c^2 \mu} \mathbf{D} \mathbf{u}_i, \quad (10.1)$$

where  $\mathbf{u}_i$  is the phonon eigenvector of the mode  $i$  with frequency  $\omega_i$ ,  $\mu$  is the mass of each rigid layer per unit area,  $c = 3.0 \times 10^{10} \text{ cm} \cdot \text{s}^{-1}$  is the speed of light and  $\mathbf{D}$  is the shear or layer-breathing part of the force constant matrix. By diagonalizing the corresponding  $N \times N$  (tridiagonal) dynamics matrix, the frequency  $\omega_i$  of the  $i$ th vibrational mode is given by

$$\omega_{S,i} = \frac{1}{\pi c} \sqrt{\alpha_0^{\parallel} / \mu} \sin\left(\frac{i\pi}{2N}\right) \quad (10.2a)$$

$$\omega_{LB,i} = \frac{1}{\pi c} \sqrt{\alpha_0^{\perp} / \mu} \sin\left(\frac{i\pi}{2N}\right), \quad (10.2b)$$

where  $i = 1, 2, \dots, N-1$ . We usually denote these  $N-1$  S modes and  $N-1$  LB modes as  $S_{N,N-i}$  and  $LB_{N,N-i}$ , respectively, where  $N$  is the layer number and  $i$  is the number of phonon branches. The  $i=N-1$  branch, i.e.,  $S_{N1}$  and  $LB_{N1}$ , corresponds to the modes with the highest frequency, whereas the  $i=1$  branch, i.e.,  $S_{N,N-1}$  and  $LB_{N,N-1}$ , correspond to the modes with the lowest frequency. The corresponding  $i$ th displacement eigenvector  $v_j^{(i)}$  is given by

$$v_j^{(i)} = \cos\left[\frac{i(2j-1)\pi}{2N}\right], \quad (10.3)$$

where  $j$  labels the layers. Figure 10.2a, b shows the frequencies and corresponding normal mode displacements of the S and LB modes in 2-4LG, and those for MoS<sub>2</sub> are shown in Fig. 10.2c, d, in which R and IR represent Raman active and infrared active, respectively.

In the case of bulk 2DMs,  $N \rightarrow \infty$ ,  $\omega(S_{bulk}) = \frac{1}{\pi c} \sqrt{\alpha_0^{\parallel} / \mu}$  and  $\omega(LB_{bulk}) = \frac{1}{\pi c} \sqrt{\alpha_0^{\perp} / \mu}$ . Thus, the equations for  $\omega(S_{N,N-i})$  and  $\omega(LB_{N,N-i})$  can be reduced to

$$\omega(S_{N,N-i}) = \omega(S_{bulk}) \sin(i\pi/2N), \quad (10.4)$$

and

$$\omega(LB_{N,N-i}) = \omega(LB_{bulk}) \sin(i\pi/2N), \quad (10.5)$$

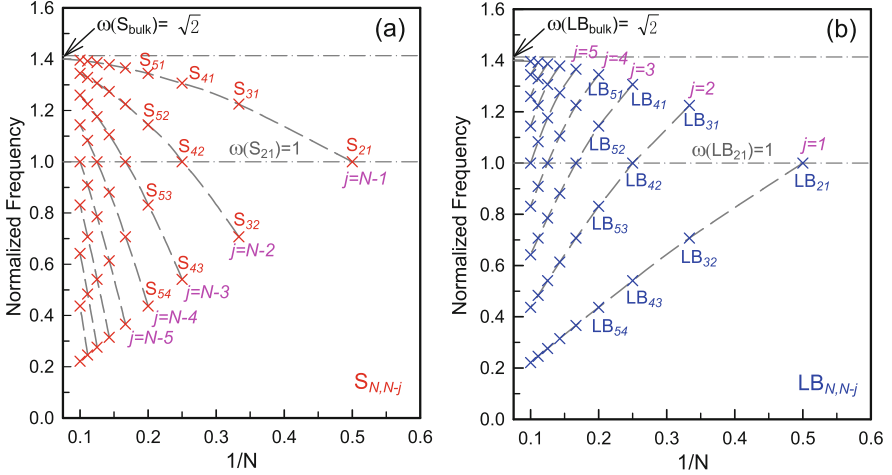


**Fig. 10.3** Frequency of the S (a) and LB (b) modes in  $NL$ -2DMs as a function of inverse  $N$ , where  $\omega(S_{21})$  and  $\omega(LB_{21})$  are normalized to 1. (Reproduced with permission from Ref. [2])

respectively. In bilayer 2DMs (2L-2DMs),  $\omega(S_{21}) = \frac{1}{\sqrt{2}}\omega(S_{bulk})$ ,  $\omega(LB_{21}) = \frac{1}{\sqrt{2}}\omega(LB_{bulk})$ . That is, once the  $\omega(S_{bulk})$  and  $\omega(LB_{bulk})$  are normalized to  $\sqrt{2}$ ,  $\omega(S_{21})$  and  $\omega(LB_{21})$  is equal to 1. Figure 10.3a shows the branches ( $i = N-1, N-2, \dots$ ) for the S modes, and Fig. 10.3b shows the branches ( $i = 1, 2, \dots$ ) for the LB modes.

The LCM provides a convenient way to describe the interlayer Raman modes in 2DMs, and once the frequencies of the bulk materials are ascertained, the frequencies of the interlayer modes in the corresponding  $NL$ -2DMs can be determined. This method can be extended to the 2D alloys and the heterostructures. Based on  $\omega(S_{bulk})$ , the shear modulus can be obtained by multiplying  $\alpha_0^{\parallel}$  with the interlayer distance. For  $\text{MoS}_2$ ,  $\omega(S_{bulk}) \sim 32.5 \text{ cm}^{-1}$ ,  $\mu = 3.0 \times 10^{-7} \text{ g cm}^{-2}$ , so the interlayer force constant  $\alpha_0^{\parallel} = 2.82 \times 10^{19} \text{ N/m}^3$  and the shear modulus is  $\sim 18.9 \text{ GPa}$ . The shear modulus of other typical 2DMs, as well as the in-plane constants ( $a$ ), interlayer distance ( $d$ ),  $\omega(S_{bulk})$ , and interlayer force constant per unit area for the S modes ( $\alpha_0^{\parallel}$ ) are summarized in Table 10.2 [2].

As discussed above, only the nearest-neighbor interlayer coupling is considered in the LCM. However, in some special 2DMs, such as MLG and tMLG, the LCM with only nearest-neighbor interlayer interactions may be insufficient for reproducing the frequencies of the LB modes [14]. Then, it is necessary to introduce an interlayer force constant between the next-nearest neighbor layers in the LCM, which is referred as 2LCM. This will be discussed in detail in the Chap. 1 on the Raman spectroscopy of graphene materials.



**Table 10.2** In-plane lattice constant ( $a$ ), interlayer distance ( $d$ ),  $\omega(S_{bulk})$ , interlayer force constants per unit area ( $\alpha_0^{\parallel}$ ), shear modulus ( $C_{44}$ ) determined by the C mode frequency and that ( $C_{44}^*$ ) obtained by other methods

Crystal	$a$ ( $10^{-8}$ cm)	$d$ ( $10^{-8}$ cm)	$\omega(S_{bulk})$ ( $\text{cm}^{-1}$ )	$\alpha_0^{\parallel}$ ( $10^{19}$ N/m <sup>3</sup> )	$C_{44}$ (GPa)	$C_{44}^*$ (GPa)
MoS <sub>2</sub>	3.15	6.15	32.5	2.82	18.9	18.6 <sup>a</sup>
MoSe <sub>2</sub>	3.29	6.46	25.5	2.60	16.8	
WS <sub>2</sub>	3.18	6.25	27.5	3.16	19.7	
WSe <sub>2</sub>	3.28	6.48	23.8	3.06	19.8	
GaSe	3.75	7.96	19.3	1.44	11.5	$9.0 \pm 1^b$
GaS	3.59	7.75	22.4	1.38	10.6	$9.96 \pm 0.15^b$
CuS	3.79	8.17	19.3	1.73	14.2	
Graphite	2.46	3.35	43.5	1.28	04.3	4.6 <sup>c</sup>
BN	2.50	3.33	52.2	1.83	06.1	
NbSe <sub>2</sub>	3.44	6.27	28.4	2.92	18.3	19.0 <sup>a</sup>
GeSe	4.38 <sup>d</sup>	5.41	40.0 <sup>f</sup>	4.26	23.1	
GeSe	3.83 <sup>e</sup>	5.41	39.0 <sup>g</sup>	4.05	21.9	
Bi <sub>2</sub> Te <sub>3</sub>	4.38	2.61	25.46	4.57	11.93	
Bi <sub>2</sub> Se <sub>3</sub>	4.14	2.58	17.96	5.26	13.57	
ReSe <sub>2</sub>	6.7 <sup>h</sup> /6.6 <sup>i</sup>	6.70	17.11/18.67	1.78/1.94	11.96/13.04	
ReS <sub>2</sub> <sup>j</sup>	6.38/6.52	6.20	24.75/19.52	2.54/1.55	15.75/9.61	
ReS <sub>2</sub> <sup>k</sup>	6.43/6.52	6.20	21.35	1.89	11.72	

<sup>a</sup>Ref. [22]<sup>b</sup>Ref. [23]<sup>c</sup>Ref. [24]<sup>d</sup> $c = 4.38$ <sup>e</sup> $b = 3.83$ <sup>f</sup>Along  $c$  axis<sup>g</sup>Along  $b$  axis<sup>h</sup>Along  $a$  axis<sup>i</sup>Along  $b$  axis<sup>j</sup>Anisotropic-like structure<sup>k</sup>Isotropic-like structure

### 10.3 Techniques for ULF Raman Spectroscopy

Compared with the intralayer vibrations in high-frequency regions, the interlayer modes are usually much lower in frequency ( $< 100 \text{ cm}^{-1}$ ) and closer to the Rayleigh line, the measurements of which are limited in the Raman system with a monochromator and a notch or edge filters. In recent years, in order to access the ULF Raman signal, several techniques have been applied to the confocal Raman system [25–31]. Here, we only introduce two typical Raman setups for ULF detection: multiple cascaded monochromators [32–35] and single monochromators with notch filters (NFs) based on volume Bragg grating (VBG) techniques [13, 14, 21].

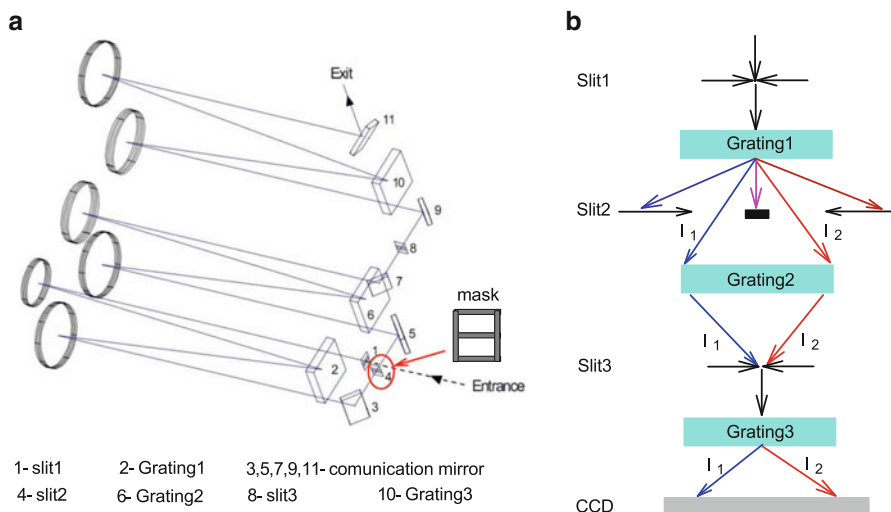


**Fig. 10.4** Diagram of products (a) and a schematic (b) of the tri-grating spectrometer

The standard apparatus to access a Raman signal in the ULF region is to use a subtractive mode of double or triple cascaded high-resolution monochromators, which provides flexible operations down to  $5\text{--}10\text{ cm}^{-1}$  at different wavelengths [31, 36]. Figure 10.4a shows a diagram of the products in the triple grating spectrometer and Fig. 10.4b is its schematic diagram. The tri-grating spectrometer consists of two parts, in which the first and second grating (1800 grooves/mm) together with a mask (denoted as slit2) and intermediate slit (slit3) are included in the first part to serve as a notch filter and the third grating behaves as a monochromator. The first two gratings serve as a set of aberration-corrected holographic gratings. In general, the scattering light is collected and imaged onto the entrance slit of the spectrometer. Once the scattering light traverses the first grating, it becomes spatially separated according to the various wavelengths. Then, the Rayleigh line is removed by the mask while the Raman scattering light passes through the slit without any obstructions, as shown in Fig. 10.4b. Grating2 is used to converge all the Raman scattering light together, and slit3 removes the stray light caused by diffraction from the mask. Meanwhile, this slit forms the entrance to the second part of the spectrometer. The third grating disperses the scattering light again and then the light is focused onto the detectors. If the mask is removed, the tri-grating spectrometer can serve as an additive mode to achieve superior high resolution. Although the ULF Raman signals are accessible via the multiple cascaded high-resolution monochromators [31, 36–42], the throughput of this setup is really low, at least one order of magnitude lower than that of a single monochromator, resulting in more accumulated time and limitations on potential applications in various 2DMs.

Recently, large advances of VBG-based NFs (BNFs) has enabled the detection of ULF Raman modes even when a single stage Raman spectrometer is used [21]. The

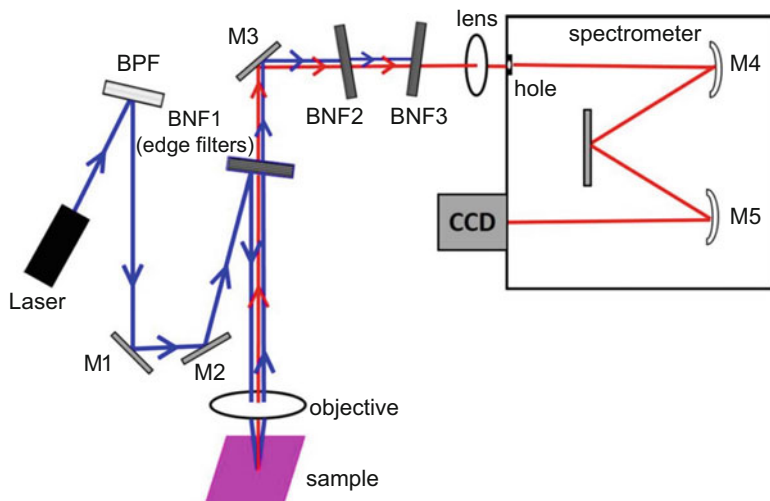


**Fig. 10.5** Schematic diagram of a single monochromator with three BNFs [21]

narrow bandwidth ( $\sim 5\text{--}10\text{ cm}^{-1}$ ) and high transmittance (up to 80–90% depending on the laser wavelength) for each filter make it possible to measure ULF Raman signals with a high signal-to-noise ratio via easy operation. To effectively reject the Rayleigh line, 3–4 VBG-based NFs with an optical density of 3 or 4 and a spectral bandwidth of  $\sim 5\text{--}10\text{ cm}^{-1}$  are usually used. The modified configuration of the three BNFs in a single monochromator is shown in Fig. 10.5 and a similar arrangement can be implemented for other spectrometers. The spectral width of VBG-based bandpass filters (BPFs) can be as small as  $5\text{--}10\text{ cm}^{-1}$  to remove the plasma lines of the lasers. Because the BPF is a reflecting filter, at least two mirrors are necessary to align the laser excitation to the center of the BNFs. The excitation light is then focused on the samples and at the same time the scattered light including the Rayleigh line is collected by the objective. Three BNFs are usually well tuned to reach deep blocking at the laser line up to OD  $\sim 9\text{--}12$ . Afterwards, the ULF Raman signals are effectively and selectively guided into the monochromator. The throughput of the Raman setup with this configuration is much higher than that of the tri-grating spectrometer. This setup has been used to probe the S modes of AB-MLGs [21], the ULF interlayer vibrations in various 2DMs [13, 14, 43–47] and the acoustic phonons in nanostructures [48]. Recently, ULF Raman measurements down to  $2\text{ cm}^{-1}$  have been accessible at 488 nm excitation, approaching the Brillouin scattering region [49].

In addition, the greater the number of BNFs that are used to obtain fine laser line attenuation, the lower the transmittance for the ULF Raman signals will be. This implies that a monochromator with BNFs may be limited in detecting very weak ULF Raman modes. Thus, a new Raman configuration with nano-edge longpass filters has been introduced [50]. The ULF Raman modes down to  $10\text{ cm}^{-1}$  can be

detected with high throughput and easy operation via this Raman system. Moreover, a cross-polarized backscattering geometry can be used to suppress the Rayleigh signal and obtain Raman spectra very close to the laser line, significantly enhancing the signal-to-noise ratio.

## 10.4 ULF Raman Spectroscopy of 2DMs

### 10.4.1 *N*-Dependent ULF Raman Spectroscopy in Isotropic *NL*-2DMs

As elucidated in Sect. 10.2, the frequencies of the S and LB modes in bulk 2DMs and 2L-2DMs are directly related to  $\alpha_0^{\parallel}$  and  $\alpha_0^{\perp}$ , therefore, one can obtain all the frequencies of the S and LB modes in *NL*-2DMs via the LCM once the S and LB modes are detected in 2L-2DMs and bulk counterpart. Thus, the LCM provides a convenient way to describe the interlayer Raman modes in 2DMs and this method can be extended to various 2DMs, including 2D crystals, 2D alloys and vdWHs. The intralayer force constants in each rigid layer are much larger than  $\alpha_0^{\parallel}$  and  $\alpha_0^{\perp}$ . They can be revealed from the frequencies of intralayer optical phonons in 1L-2DMs, [44]. Take in-plane isotropic MoS<sub>2</sub> as an example, based on the diatomic chain model (DCM), [44] the relative displacements between molybdenum and the sulfur layers in the rigid S-Mo-S trilayer are very small for all S and LB modes,  $\sim 0.6\%$  in 2L-MoS<sub>2</sub>, and the relative displacement decreases with increasing *N*. Thus, all the atoms in each rigid S-Mo-S trilayer can be considered a single ball with a mass of  $M = m_{Mo} + 2m_S$ . The balls are coupled with each other by the interlayer coupling of  $\alpha_0^{\parallel}$  ( $\sim 2.82 \times 10^{19}$  N/m<sup>3</sup>) for the S modes and of  $\alpha_0^{\perp}$  ( $\sim 8.9 \times 10^{19}$  N/m<sup>3</sup>) for the LB modes, which can be deduced from the peak positions of the S<sub>21</sub> and LB<sub>21</sub> modes in 2L-MoS<sub>2</sub> and the  $S_{bulk}$ , LB<sub>bulk</sub> mode in bulk MoS<sub>2</sub>. The eigen-equations related to the *N*-dependent interlayer vibrations can be analytically solved from Eqs. 10.4 and 10.5. Figure 10.6a shows the calculated frequencies of the branches ( $i = N-1, N-2, \dots$ ) of the S modes and Fig. 10.6b shows those of the branches ( $i = 1, 2, \dots$ ) of the LB modes in *NL*-MoS<sub>2</sub> based on the LCM and the DCM. Figure 10.6c depicts the Raman spectra of the S and LB modes in 1–20L MoS<sub>2</sub>, whose experimental frequencies are summarized in Fig. 10.6a, b in circles. The sizes of the circles indicate the relative intensities of the corresponding modes. The experimental results are in consistent with those from the LCM and DCM, indicating that the interactions between MoS<sub>2</sub> flakes and substrate are sufficiently weak to be neglected. Furthermore, it is easy to indicate that the S modes in *NL*-MoS<sub>2</sub> primarily come from the branches of  $i = N-1, N-3, N-5$ , whereas the LB modes primarily come from the branches of  $i = 1, 3, 5$ , with the result that the frequencies of the S and LB modes in the Raman spectra undergo an opposite tendency with increasing *N*. In bulk materials, the LB mode is Raman inactive and the S mode at 34 cm<sup>-1</sup> is Raman active. The peak positions and FWHM of the S<sub>N1</sub>

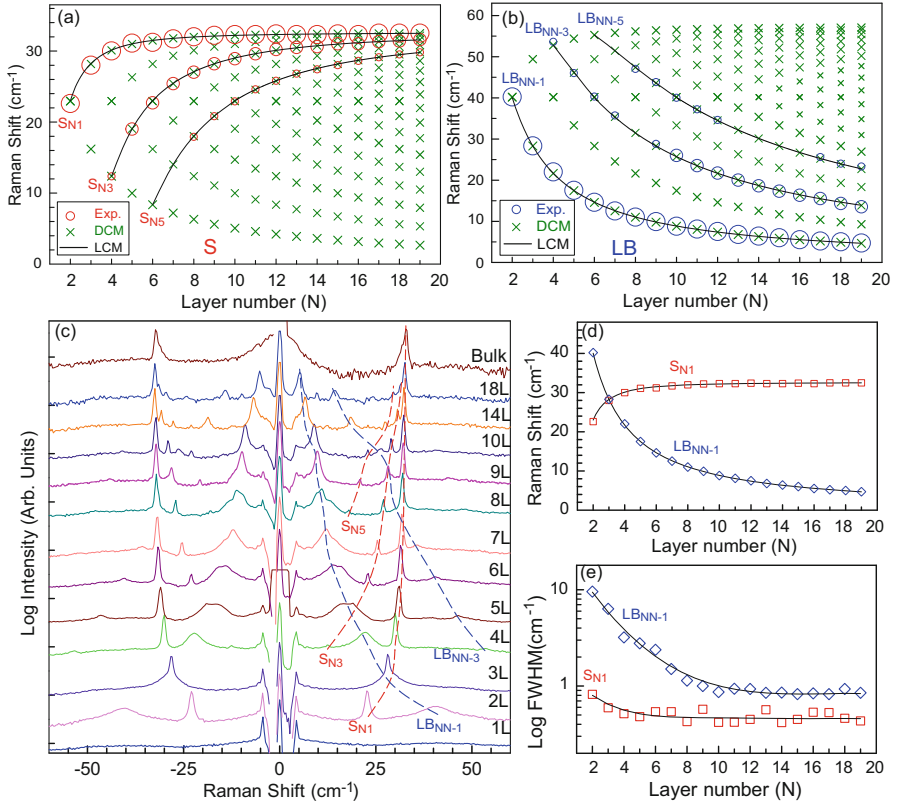


**Fig. 10.6** Peak positions of the (a) S and (b) LB modes of  $NL$ - $\text{MoS}_2$  as a function of  $N$ . The circles are the experimental peak positions whose diameters indicate the Raman intensity of each mode. The crosses are the results from the DCM, whereas the solid lines are partial results from the LCM. (c) Stokes and anti-Stokes Raman spectra of  $NL$ - $\text{MoS}_2$  ( $N=1$ –10L, 14L, 18L) and bulk  $\text{MoS}_2$ . (d) Peak positions and (e) FWHM of the  $S_{21}$  and  $LB_{21}$  modes as a function of  $N$ . (Reproduced with permission from Ref. [44])

and  $LB_{N-1}$  modes are also represented in Fig. 10.6d, e, respectively. The peak positions of these two branches are in good agreement with those from the LCM. The larger FWHM of the LB modes compared with the S modes can be interpreted as an anharmonic feature of the LB modes with a significant enhancement of phonon-phonon scattering with decreasing  $N$ .

The symmetry of  $\text{MoS}_2$  flakes determines whether the S and LB modes are Raman active in  $NL$ - $\text{MoS}_2$ , whereas the intensity of these modes depends on the Raman scattering configurations and the electron-phonon coupling (EPC). Here we only give a detailed explanation of the symmetry and Raman scattering configurations because the calculation of EPC is very complicated. As respect to the irreducible representation from symmetry there are  $\frac{N-1}{2}(E' + E'')$  for the S modes

and  $\frac{N-1}{2}(A'_1 + A''_2)$  for the LB modes in ONL-MoS<sub>2</sub> whereas there are  $\frac{N}{2}E_g + \frac{N-2}{2}E_u$  for the S modes and  $\frac{N}{2}A_{1g} + \frac{N-2}{2}A_{2u}$  for the LB modes in ENL-MoS<sub>2</sub>.  $E'$ ,  $E''$ ,  $A'_1$ ,  $A_{1g}$  and  $E_g$  are Raman active, whereas  $E_u$  and  $A_{2u}$  are infrared active and  $A''_2$  is silent, indicating that  $E_u$ ,  $A_{2u}$  and  $A''_2$  cannot be detected via Raman spectroscopy.

Even the Raman active modes are not always observed in Raman spectra. For example, the Raman tensor of the  $E''$  mode can be written as

$$R(E'') = \begin{pmatrix} 0 & 0 & 0 \\ 0 & 0 & c \\ 0 & c & 0 \end{pmatrix} \quad (10.6)$$

Under the backscattering configuration, assuming the wavevectors of the incident and scattering light are  $\vec{e}_i = (\cos\theta, \sin\theta, 0)$  and  $\vec{e}_s = (\cos\delta, \sin\delta, 0)$ , the Raman intensity of the  $E''$  mode is

$$I(E'') \propto \left| \vec{e}_s \cdot R \cdot \vec{e}_i^T \right|^2 = 0 \quad (10.7)$$

Thus,  $I(E'')$  is always zero in the backscattering configuration.

Other TMDs show structure and symmetry similar to MoS<sub>2</sub> flakes, indicating that the above discussions can be applied to these materials by replacing the  $\omega(LB_{21})$  and  $\omega(S_{21})$  with the corresponding values of other 2L-TMDs. This is also true for all the in-plane isotropic 2DMs. However, whether they are observable in Raman spectroscopy requires detailed analysis of their symmetries, Raman tensor and EPC.

#### 10.4.2 *Stacking-Order Dependent ULF Raman Spectroscopy in Isotropic 2DMs*

The stacking order in few-layer 2DMs results in different structural symmetries and layer-to-layer interactions, and thus paves a way to controlling their electronic and optical properties. Indeed, the stacking order governs the symmetry and afterwards the Coulomb interactions, which are crucial for mediating novel physical properties, such as the semiconductor-to-metal transition, valley polarization, superconductivity, magnetism, and the charge density wave [51–55]. For example, AB-3LG is semi-metallic similar to a monolayer, whereas ABC-3LG is predicted to be a tunable band gap semiconductor under an external electric field. Interest in stacking effects has been rejuvenated with these phenomena emerging in few-layer 2DMs, which provides one more way to modify the properties, making 2DMs a promising material for next-generation electronics and optoelectronics. Before taking good control of the 2DMs with various stacking orders, it is crucial to develop a simple and powerful way to distinguish these different stacking sequences in 2DMs. ULF Raman spectroscopy is most often used for stacking-order characterizations.

Although the most recent studies in 2DMs focus on the AB stacking or 2H stacking phase, the stacking effects on the interlayer Raman modes have intrigued many researchers, [53, 56, 57] leading to an in-depth understanding of stacking phases, including that of 2H, 3R and 1T (Fig. 10.1b) and their mixtures. The so-called AB and ABC stackings are also named 2H and 3R in TMDs, respectively. TMDs are usually denoted  $\text{MX}_2$ . Among these three common phases, 2H and 3R are the most stable and can coexist in 2DM flakes grown via chemical vapour deposition (CVD), whereas the 1T-structure is “metastable” and infrequent in most natural 2DMs. Therefore, here by stating the stacking order, we refer to a traditional way to define 2H- and 3R-stacking sequences.

The first difference between these various stacking orders is in their symmetries. The space group of AB-*N*LG depends strongly on *N*, in which  $D_{3h}$  for ONLG and  $D_{3d}$  for ENLG (see Sect. 10.2 for details). In contrast to AB-*N*LG, ABC-*N*LG belongs to  $D_{3d}$  [42, 58]. Furthermore, the symmetries of *N*L 2H- $\text{MX}_2$  also depends on *N*, which are similar to the *N*LG (as shown in Table 10.1). However, with respect to the *N*L 3R- $\text{MX}_2$ , the symmetry reduces to  $C_{3v}$ . The differences in symmetry can lead to different assignments of each S and LB modes and thus different Raman activity, indicating that the ULF Raman spectroscopy will be significantly distinct, e.g.,  $S_{N1}$  are observable in AB-*N*LG but not in ABC-*N*LG due to the Raman-inactivity or weak EPC [58]. Second, various stacking orders may result in different relative displacements between the adjacent layers which have a good effect on the individual bond polarizabilities. According to the bond polarizability model, the Raman intensities are closely related to the individual bond polarizabilities, [56, 59] implying that different intensity trends of the Raman-active ULF modes are seen in different stacking orders. Using the polarizability model, the highest-frequency S mode is predicted to have the largest Raman intensity, whereas the lowest-frequency S mode in 2H-stacked 2DMs has no intensity. And the trend is opposite in the 3R-stacked systems [42, 56, 59]. Hereafter, we will show the stacking-order dependent ULF Raman spectroscopy in detail, taking  $\text{MoSe}_2$  as an example [56]. The stacking-order dependent ULF Raman spectroscopy in MLGs is referred to in Chap. 1 on Raman spectroscopy of monolayer and multilayer graphenes.

Figure 10.7a shows two schematics of representative stacking sequences of 2L- $\text{MoSe}_2$ , 2H and 3R. Apart from the layer shift, the second layer in 2H- $\text{MoSe}_2$  is rotated by  $180^\circ$  relative to the first layer. The ULF Raman modes of mechanically exfoliated and CVD-grown  $\text{MoSe}_2$  in the  $\bar{z}(xy)z$  configurations are represented in the Fig. 10.7b, c, respectively. All the observed ULF modes can be assigned as S modes because the LB modes cannot be seen under this configuration, which is determined by the symmetry and the Raman tensor [14]. Here, for brevity, the branches of the S modes are labelled  $S_1, S_2, \dots$ , in order of decreasing frequency, in accordance with the labels stated before. The exfoliated *N*L- $\text{MoSe}_2$  are in 2H stacking, considering that it is derived from a single crystal that is also of 2H stacking. In contrast to the 2H stacking, in which only the odd S modes ( $S_1, S_3, S_5, \dots$ ) are observable, more S modes can be seen in the CVD-grown  $\text{MoSe}_2$ , which implies that more stacking orders co-exist in the CVD-grown flake, as previously reported [60]. From the bond polarizability, the observed S modes in 2H- $\text{MoSe}_2$



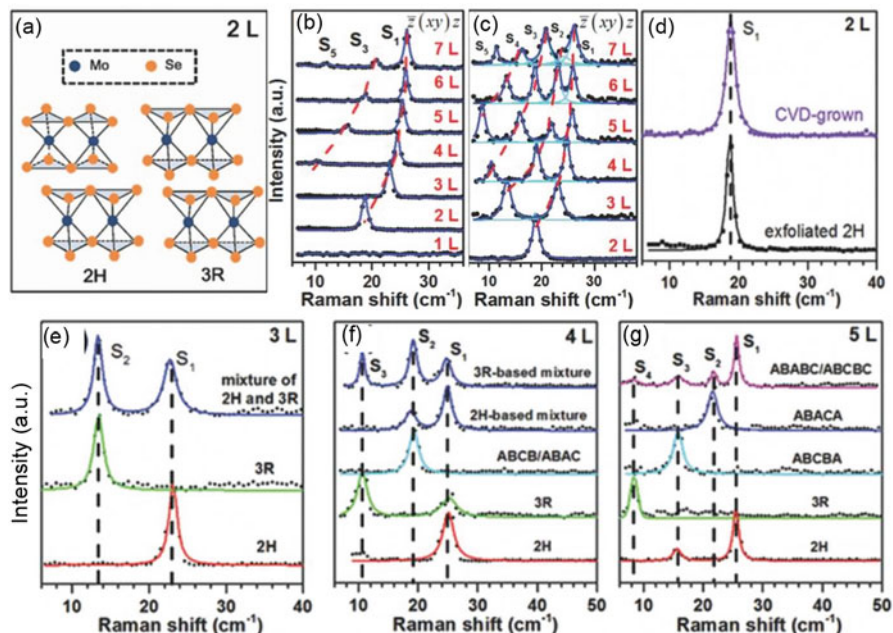


**Fig. 10.7** (a) Schematics of 2H- and 3R- MoSe<sub>2</sub> in 2L. The ULF Raman spectra of (b) exfoliated and (c) CVD-grown MoSe<sub>2</sub> with the layer number ranging from 1L to 7L in  $\bar{z}(xy)z$  configurations. Raman modes in the ULF region of CVD-grown (d) 2L, (e) 3L, (f) 4L and (g) 5L with different stackings. (Reproduced with permission from Ref. [56])

exhibit a Raman intensity trend that should behave as:  $I(S_1) > I(S_3) > I(S_5)$ , whereas those in 3R-MoSe<sub>2</sub> exhibit exactly the opposite trend [59]. The Raman intensity trend shown in Fig. 10.7c indicates the corresponding samples should have a coexistence of 2H and 3R. From the analysis above, it is easy to identify the stacking sequences from the ULF Raman modes by comparing the frequencies of the observed Raman modes and the Raman intensity trends. As depicted in Fig. 10.7d, because there is only one S mode in 2L-MoSe<sub>2</sub>, it seems difficult to distinguish the 2H and 3R stackings in 2L-MoSe<sub>2</sub>. Puretzky et al. found that the absolute Raman intensity of the S<sub>1</sub> modes in 2H-MoSe<sub>2</sub> is much larger than that in 3R stacking [61], which paves a new way to clarifying 2L-MoSe<sub>2</sub> in 2H and 3R stacking. Figure 10.7e–g shows the ULF Raman spectroscopy of 3–5L MoSe<sub>2</sub> with 2H, 3R stacking and their mixtures, which further confirms the Raman intensity trend stated above. Other than 2H and 3R stacking, more stacking orders appear as  $N$  increases. And the main stacking order of MoSe<sub>2</sub> can be distinguished from the difference in Raman intensity trend of S modes between 2H and 3R stackings. For example, considering a 4L-MoSe<sub>2</sub> flake, if the Raman intensity of S<sub>1</sub> mode is larger than that of S<sub>3</sub> mode, the stacking order of this flake can be referred to as 2H-based mixture. This can be extended to all TMDs with various stacking orders. Moreover,



the ULF Raman spectroscopy in various stacking orders can be varied from each other based on the bond polarizability model or density functional theory (DFT) calculations [56].

Notably, the characterizations of stacking order are not only applicable in MoSe<sub>2</sub> but can also be applied to other 2DMs. The correlations between the stacking order and ULF Raman spectroscopy are increasingly developed in more and more isotropic 2DMs, such as graphene [42, 58] and MoS<sub>2</sub> [53, 57], which sheds light on the potential applications of 2DMs in the optoelectronics devices.

### 10.4.3 *ULF Raman Spectra of In-Plane Anisotropic 2DMs*

Various novel physical properties of isotropic 2DMs can be modulated via the layer number and stacking order, as depicted in Sects. 10.4.1 and 10.4.2. In-plane anisotropic 2DMs, such as BP, SnSe, ReSe<sub>2</sub> and ReS<sub>2</sub>, offer one more degree of freedom to tune the interlayer coupling and thus the optoelectronic properties. The strong in-plane anisotropy in these 2DMs has been proposed for developing new devices with promising properties, which enhances their potential applications in electronics [62] and optoelectronics [63]. Until now, the anisotropic 2DMs can be divided into two categories: one category has strongly buckled honeycomb sheets with 'troughs' running along the  $y$ -axis ( $\mathbf{b}$  direction), to which BP and SnSe belong [64–66]; the second category can be considered disordered 1T'-structures. In contrast to the commonly seen 1T- or 2H-structures in TMDs with high symmetry, 1T'-structures own extra in-plane metal-metal bonds or charge density wave states, typical examples of which are WTe<sub>2</sub>, ReSe<sub>2</sub> and ReS<sub>2</sub> [45, 67, 68]. This 1T' structure, different from the 2H and 3R symmetry in the MoS<sub>2</sub>, would lead to random stacking of ReSe<sub>2</sub> (ReS<sub>2</sub>). Owing to the random stacking in ML-ReSe<sub>2</sub> (ReS<sub>2</sub>), the symmetry reduces from  $C_i$  (monolayer) to  $C_1$  (multilayer), with the result that all the Raman modes including the interlayer modes are Raman active. However, the random stacking also results in weaker interlayer modes in the thicker samples and no observable interlayer modes in bulk materials due to an increasing disorder [45]. In principle, there exist one or more stacking orders for these materials. Qiao et al. revealed two stable stacking orders in ReS<sub>2</sub>, namely isotropic-like (IS) and anisotropic-like (AI) NL according to the in-plane isotropic and anisotropic features, respectively, in ULF Raman spectra [47].

In a monolayer 1T' structure such as ReS<sub>2</sub>, a unit cell contains four formula units, including two categories of Re atoms and four categories of S atoms. In addition, the Re atoms are sandwiched by the two S atoms. Owing to the Peierls distortion [69], adjacent Re atoms are bonded in the form of zigzag four-atom clusters, which align along the direction of the lattice vector  $\mathbf{a}$  to form Re chains. Figure 10.8a, b represented the schematics of AI-2L-ReS<sub>2</sub> and IS-2L-ReS<sub>2</sub>. As shown in the left panel of Fig. 10.8a, b, the Re-Re bond in a unit cell is almost oriented parallel to the direction  $\mathbf{b}$ , and the top S atoms with these two Re atoms are in the forward direction  $\mathbf{a}$ , forming the Re-S-Re triangle. The triangle can be chosen to address

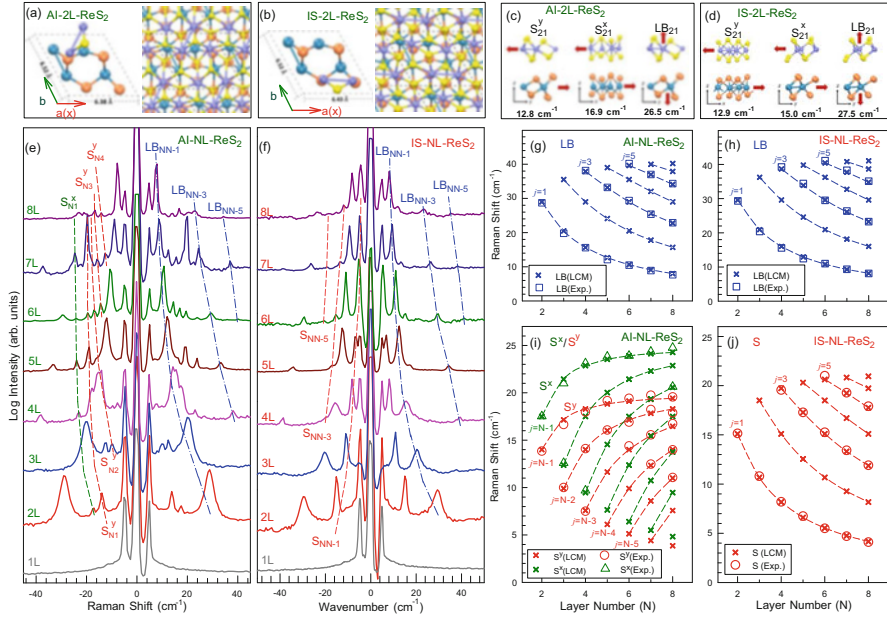


**Fig. 10.8** Stacking schematic diagrams and the top view of the crystal structure of AI-2L-ReS<sub>2</sub> (a) and IS-2L-ReS<sub>2</sub> (b). The atomic displacements schematics and the corresponding frequencies of three ULF interlayer modes in AI- (c) and IS-stacked structures (d) obtained from DFT calculation are also shown. (e) and (f) are the Stokes/anti-Stokes ULF Raman spectra for AI-NL-ReS<sub>2</sub> and IS-NL-ReS<sub>2</sub> with the layer number ranging from 1L to 8L, respectively. The dashed lines are guides to the eyes for S modes and LB modes. Frequencies of LB modes as a function of  $N$  in AI- (g) and IS-stacked (h) ReS<sub>2</sub>. The corresponding relation for S modes in AI- (i) and IS-stacked structures (j) are also shown. The squares, triangles and circles are the experimental data, and the crosses are from the calculations based on the LCM. (Reproduced with permission from Ref. [47])

the structural symmetry of  $NL$ -ReS<sub>2</sub>. For 2L-ReS<sub>2</sub>, the Re-Re bond of the top layer has three possible orientations: 0°, 60° and 90° with a given symmetry of the bottom layer. Furthermore, there are four possible relative positions of the two Re-Re bonds of both layers for each orientation, resulting in a total of 12 stacking orders. Among these stacking sequences, AI-2L-ReS<sub>2</sub> is the most stable configuration according to the DFT calculations, whereas IS-2L-ReS<sub>2</sub> is the second most stable configuration. As shown in Fig. 10.8a, b, the Re-Re bond in the top layer of AI-2L-ReS<sub>2</sub> is oriented 60°, whereas it is almost parallel to the  $a$  axes in IS-2L-ReS<sub>2</sub>. Although the projection of these two bonds appears symmetric, the bilayer geometry is not exactly identical along the  $a$  and  $b$  axes, which is indicated by the fully relaxed lattice constants of 6.43 ( $a$ ) and 6.52 ( $b$ ).

For anisotropic 2DMs, the two axes in the basal 2D plane are not equal, with the result that the S modes along the two axes are not degenerate. Thus, there are  $2(N-1)$  S modes and  $N-1$  LB modes in  $NL$  anisotropic 2DMs, in which the S modes can be

divided into two categories based on their vibrational directions ( $x$ ,  $y$ ). Figure 10.8c, d show the vibrational displacements and the corresponding frequencies of the S modes along  $x$ ,  $y$  directions and the LB modes. In AI-2L-ReS<sub>2</sub>, the theoretical frequencies of the S and LB modes are  $\omega(S_{21}^y) = 12.8 \text{ cm}^{-1}$  and  $\omega(S_{21}^x) = 16.9 \text{ cm}^{-1}$ , whereas  $\omega(LB_{21}) = 26.5 \text{ cm}^{-1}$ . The frequency difference between two S modes is  $4.1 \text{ cm}^{-1}$ , which is larger than the FWHM of the S modes. This means that they can be distinguished in the ULF Raman spectrum. Indeed, not only the frequency difference but also the absolute values of the S and LB modes are in good agreement with those from the experiment, as shown in Fig. 10.8e. In contrast, the theoretical frequency difference between the two S modes is  $2.1 \text{ cm}^{-1}$  in IS-2L-ReS<sub>2</sub>, which is only half the experimental result and comparable with the FWHM of the S mode, leading to the overlap of these two S modes in Raman spectroscopy, as depicted in Fig. 10.8f. In addition, the LB modes in these two stacked structures are quite close to each other, it is  $1.0 \text{ cm}^{-1}$  softer in the AI-2L-ReS<sub>2</sub>. Moreover, for ReS<sub>2</sub> with a given  $N$ , there are two categories of ULF Raman modes, as shown in Fig. 10.8e, f. Similar to bilayer ReS<sub>2</sub>, these two categories correspond to the AI- and IS- stacking structures. Based on the LCM stated in Sect. 10.2, these interlayer modes can be expressed by the  $S_{21}$  and  $LB_{21}$  modes (see Eqs. 10.4 and 10.5 in Sect. 10.2). Based on LCM, all the ULF Raman modes in isotropic 2DMs can be predicted by  $\text{Pos}(S_{21})$  and  $\text{Pos}(LB_{21})$ . This is also the case for anisotropic 2DMs, by replacing the  $S_{NN-i}$  and  $S_{21}$  with  $S_{NN-i}^x$ ,  $S_{NN-i}^y$  and  $S_{21}^x$ ,  $S_{21}^y$ , respectively. All the LB modes in AI-NL-ReS<sub>2</sub> and IS-NL-ReS<sub>2</sub> as well as those from calculations are summarized in Fig. 10.8g, h. Comparing the experimental and theoretical results, it can be deduced that only the  $LB_{NN-1}$ ,  $LB_{NN-3}$  and  $LB_{NN-5}$  (indicated by the dash lines) are observable in both stacking structures. With respect to the S modes in AI-NL-ReS<sub>2</sub> and IS-NL-ReS<sub>2</sub>, the frequencies are also summarized in Fig. 10.8i, j. There are two categories of S modes in AI-NL-ReS<sub>2</sub> as previously predicted, in which the interlayer vibrations along the  $x$  ( $S^x$  modes) and  $y$  ( $S^y$  modes) directions are marked by the dash lines, as demonstrated in Fig. 10.8a. The observed branch for the  $S^x$  modes is  $i = N-1$ , whereas for the  $S^y$  mode the observed branches are  $i = N-1, N-2, N-3$  and  $N-4$ . However, in IS-stacking structures, only the  $S_{NN-i}$  branches with  $i = 1, 3, 5$  can be detected and each branch decreases in frequency with increasing  $N$ , similar to the corresponding LB modes. This is ascribed to the different symmetries and EPC between the AI and IS-stacking structures.

On the other hand, with the given frequencies of interlayer modes, it is easy to determine the interlayer coupling 2DMs, such as ReS<sub>2</sub>. The interlayer force constant can be written as  $\alpha_0^{\parallel} = (2\pi^2 c^2) \mu (\omega(S_{21}))^2$  and  $\alpha_0^{\perp} = (2\pi^2 c^2) \mu (\omega(LB_{21}))^2$ . From the experimental  $S_{21}^x$  and  $S_{21}^y$ , the  $\alpha_0^{\parallel}$  along the  $x$  and  $y$  directions are  $\sim 90\%$  and  $\sim 55\%$  to those of 2L-MoS<sub>2</sub>, respectively, whereas in the IS-stacking structure,  $\alpha_0^{\parallel}$  is only 67% of that in 2L-MoS<sub>2</sub>. Considering  $\alpha_0^{\perp}$  in both stacking structures, it is approximately 76% to that in 2L-MoS<sub>2</sub>. All these results indicate that the interlayer interactions in AI- and IS-NL-ReS<sub>2</sub> are comparable with those in other 2DMs, which deviates from the previous predictions that ReS<sub>2</sub> lacks interlayer coupling. The revealed strong interlayer coupling and polytypism in NL-ReS<sub>2</sub> stimulate

further studies on tuning the novel properties of other anisotropic 2DMs and paves the way to enhancing their potential applications in next-generation electronic or optoelectronic devices with superior characters. In addition, BP is one of the most popular anisotropic 2DMs and has intrigued many researchers. However, it is easily oxidized in air, which significantly suppresses its investigations and applications.

#### 10.4.4 ULF Raman Spectra of Twisted 2DMs

Stacking 2DM flakes can serve the assembly of the artificially structured vdWHs, thus the fundamental properties and potential applications of 2DM flakes have recently attracted the attention of many researchers [5]. Hereafter, we will discuss how the interlayer coupling and ULF Raman modes modulate in two classical types of artificial 2DMs, i.e., twisted 2DMs (this section) and heterostructures (next Sect. 10.4.5). They vary from each other with component types. The twisted 2DMs are structured by stacking the same type of 2DM flakes with different crystal orientations, whereas the heterostructures usually consist of several types of 2DMs.

By assembling an  $mL$ -2DM flake on the same type of  $nL$ -2DM flake, an  $(m+n)L$ -2DM system is formed, which is commonly denoted as  $t(m+n)L$ -2DM, such as  $t(m+n)LG$  and  $t(m+n)L-MoS_2$ . Note that when we are discussing twisted 2DMs, its constituents are always assumed to be in the most stable or natural structure, e.g., Bernal (AB) stacked MLG and 2H-TMDs. The choice for  $m$ ,  $n$  and the twist angle ( $\theta_t$ ) between each  $mL$ -,  $nL$ -, ...  $MoS_2$  is so immense that it generates a large family of systems with different optical, electronic and vibrational properties. It has already been reported that in gapless graphene, the interlayer coupling depends sensitively on the interlayer twist angle, and plays important roles in modifying the electronic and vibrational properties [13, 14, 50, 70]. The shear coupling at the interface of  $tMLG$  is revealed to be  $\sim 20\%$  of that in AB-MLG whereas the interlayer breathing force constant approaches  $\sim 100\%$  of that in AB-MLG. Furthermore, the Raman intensity of the S, LB and G modes in  $t(m+n)LG$  are significantly enhanced for specific excitation energies, which is attributed to the resonance between the  $\theta_t$ -dependent energies of van Hove singularities (VHSs) in the joint density of states (JDOSs) of all optically allowed transitions [13]. This is also the case in other 2DMs, such as  $MoS_2$  and  $MoSe_2$ . For  $MoS_2$ , the modified layer stacking in twisted samples can lead to a decrease in the interlayer coupling, an enhancement or quenching of the photoluminescence emission yield [71]. Thus, the tunable interlayer coupling and thus the physical properties are accessible by generating artificial twisted  $MoS_2$  with different stacking structures. As stated above, ULF Raman spectroscopy opens the door to directly detecting the interlayer coupling, which is essential to design the 2DMs with promising properties. Here, the ULF Raman modes are used to correlate the relationship between the interfacial coupling and the twisted patterns (so-called Moiré patterns) [17].

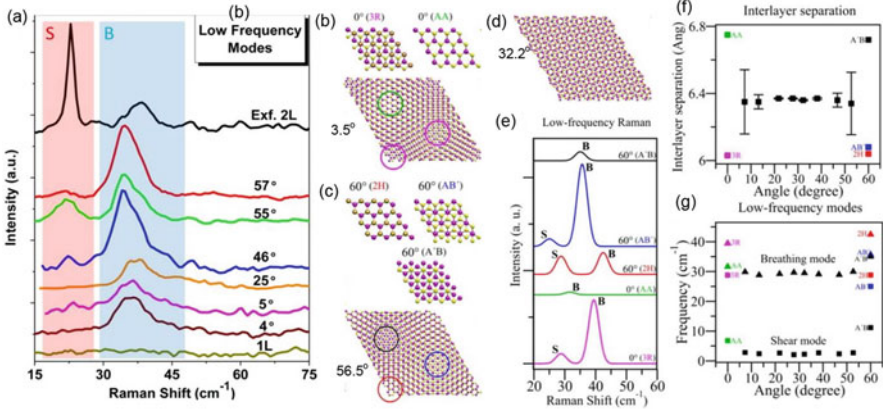


**Fig. 10.9** ULF Raman spectra of  $t(1+1)L$ - $\text{MoS}_2$  with different twist angles ranging from  $0^\circ$  to  $60^\circ$  and that of 1L, exfoliated bilayer 2H- $\text{MoS}_2$  (Exf. 2L), in which S and B denote the S and LB modes, respectively. Atomic structures of commensurate  $t(1+1)L$ - $\text{MoS}_2$  with various twist angles. There are two stacking patches denoted 3R and AA at (b)  $0^\circ$  and a mixture of these two stackings when the twisted angle deviates from  $0^\circ$ . Three stacking patches denoted 2H, AB' and A'B appear when  $\theta_t = 60^\circ$  (c) and all of these stacking patches can also coexist when  $\theta_t$  near  $60^\circ$ . When  $\theta_t$  approaches  $30^\circ$  (d), the stacking becomes completely mismatched. (e) ULF Raman spectra of different high-symmetry stacking patches from DFT calculations. The interlayer separation (f) and ULF Raman modes (g) are also shown. (Reproduced with permission from Ref. [17])

Figure 10.9a shows the typical S and LB modes of  $t(1+1)L$ - $\text{MoS}_2$  with  $\theta_t$  between  $0^\circ$  and  $60^\circ$ . The S modes in  $t(1+1)L$ - $\text{MoS}_2$  are much weaker than those in 2H- $\text{MoS}_2$ , whereas its LB modes show higher intensities. All the modes are redshifted and show an asymmetric profile when the twist angle deviates from  $0^\circ$  and  $60^\circ$ . The interlayer Raman modes show distinct features for different stacking structures. For example, the S mode is absent for certain twist angles (ranging from  $20^\circ$  to  $40^\circ$ ), similar to the results of other twisted TMDs [16]. The absence of the S mode is always attributed to the disappearance of local high-symmetry domains. To well elucidate how the twist angle affects the interlayer coupling and thus the ULF Raman modes, it is necessary to clearly depict the stacking structures with various twist angles. Figure 10.9b–d plot the schematics of the possible twisted patterns when the twisted angle is equal to  $0^\circ$ ,  $3.5^\circ$ ,  $60^\circ$ ,  $56.5^\circ$  and  $32.2^\circ$ . When  $\theta_t = 0^\circ$ , there are two high-symmetry stacking patterns 3R and AA, whereas at  $60^\circ$ , there are three possible stacking patterns denoted 2H, AB' and A'B. When the twist angles deviate from  $0^\circ$  and  $60^\circ$ , several stacking patterns can coexist in the twisted regions, as indicated by the circles in Fig. 10.9b, c. Furthermore, the patch sizes of high-symmetry configurations are seen to decrease with the twist angle deviating from  $0^\circ$  and  $60^\circ$ . For the twist angle approaching  $30^\circ$ , the stacking does not show the high-symmetry patches, which can usually be assigned to incommensurate patterns. The ULF Raman spectra for the high-symmetry stacking structures from the DFT calculations are also shown in Fig. 10.9e. Interestingly, the S and LB modes show

similar Raman intensities in the most stable 2H structures, whereas in other stacking structures, the LB mode is much stronger than the S mode. This observation is in accord with the experimental results. From 2H to other stackings, the S mode becomes weaker and the LB mode becomes stronger. In contrast to the high-frequency vibrations in which the change in the polarizability (i.e., Raman intensity) is primarily contributed by the vibrations of intralayer chemical bonds, the change in the polarizability of interlayer modes is solely due to layer-layer vibrations. Thus, the relative Raman intensities of the S and LB modes change dramatically in various stackings. Turning to  $\theta_t$  near  $0^\circ$  or  $60^\circ$ , the stacking yields a pattern composed of a mixture of multiple high-symmetry domains. The Raman intensity of the S modes in AB' and A'B stacking decreased significantly, whereas that of the LB modes increased. Hence, in t(1+1)L-MoS<sub>2</sub> with  $\theta_t$  near  $60^\circ$  (such as  $57^\circ$  and  $55^\circ$ ), the S modes become weaker and the LB modes are greatly enhanced compared with those in 2H-MoS<sub>2</sub>. For  $\theta_t$  near  $0^\circ$ , the Raman intensities of the S and LB modes follow a similar trend. This successfully explains why the S modes are weak and the LB modes are strong in t(1+1)L-MoS<sub>2</sub>.

In addition, the average frequencies of all the ULF Raman modes red shift from 2H- to t(1+1)L-MoS<sub>2</sub>, which is in line with the experiments. This result can be explained by the weaker interlayer coupling and the increase in the interlayer distance in twisted structures, as depicted by Fig. 10.9f. For  $\theta_t < 10^\circ$  or  $\theta_t > 50^\circ$ , various high-symmetry patches coexist in the overall stacking pattern, leading to distinct frequencies and intensities for the S and LB modes in t(1+1)L-MoS<sub>2</sub>. Such changes will in turn modify the relative contributions to the Raman scattering and they are also the reason why the LB modes are always seen as asymmetric. For the twisted angle between  $20^\circ$  and  $40^\circ$ , the stacking patterns are not so commensurate and thus neither rotational nor translation symmetry preserved, with the result that the interlayer coupling varies negligibly. Hence, the interlayer distance is constant and the changes in the S or LB modes are insignificant, as shown in Fig. 10.9g. The absence of local high-symmetry domains due to the mismatched stacking makes the stacking features essentially insensitive to the in-plane shear motion and thus leads to a small overall restoring force. As a result, the frequency of the S mode is so low that it appears in the background of the Rayleigh line and thus beyond the detection limit. In addition, for  $\theta_t$  ranging from  $10^\circ$  to  $20^\circ$  and  $40^\circ$  to  $50^\circ$ , the stacking arrangements are between a mixture near  $0^\circ$  and  $60^\circ$  and the mismatched stacking near  $30^\circ$ . In this region, the experimental and theoretical results sometimes deviate. To sum up, the ULF Raman spectra vary dramatically in t(1+1)L-MoS<sub>2</sub> with different twist angles, which provides a new way to identify the interlayer coupling in twsited 2DMs with various  $\theta_t$ . More specifically, the ULF Raman modes share a similar tendency in other t(1+1)L-TMDs, such as in twisted MoSe<sub>2</sub> [16].

Moreover, apart from the t(1+1)L-2DM, there is a large family of 2DMs with twisted structures due to the variety of  $m$ ,  $n$  and more constituents. However, the investigations of interlayer modes as well as the novel physical properties are still lacking and require further studies.



### 10.4.5 ULF Raman Spectra of vdWHs

With the development of material growth and transferring techniques, different types of 2DMs can be stacked onto each other to form vdWHs [72–75]. The vdWHs provides a multitude of applications because it becomes possible to create artificial materials that combine several unique properties for use in novel multi-tasking applications [76, 77]. The strong interlayer coupling in vdWHs can be revealed by the strong photoluminescence of spatially indirect transitions in MoS<sub>2</sub>/WSe<sub>2</sub> heterostructures, in which the coupling at the interface can be tuned by inserting dielectric layers such as h-BN [78]. The interlayer coupling can also directly affect the observed S and LB modes, which implies that it is one of the most powerful tools for measuring the interfacial coupling in vdWHs. The S modes are absent in the Raman spectra of MoSe<sub>2</sub>/MoS<sub>2</sub> and MoS<sub>2</sub>/WSe<sub>2</sub>, whereas the LB modes are seen in the heterostructure regions with direct interlayer contact and an atomically clean interface [75]. This is the behaviour that is expected by considering the interlayer interactions in vdWHs. The lattice mismatch between the MoS<sub>2</sub> and WSe<sub>2</sub> layers reaches to ~4%, so that the lateral displacements do not produce any overall restoring force. However, the vertical displacements can create a finite restoring force due to the vdW interaction between them. The vdWHs formed by two 2DM flakes from different categories, such as TMDs and graphene, are essential for revealing the intrinsic nature of interfacial coupling in vdWHs.

The MoS<sub>2</sub>/NLG vdWHs can be prepared by transferring MoS<sub>2</sub> flakes onto NLG flakes, or by transferring NLG flakes onto MoS<sub>2</sub> flakes [20]. In general, the annealing process is necessary after the transfer to form good interfacial coupling because the two as-transferred heterostructures may not couple with each other. However, an appropriate annealing time is very important to obtain these vdWHs with high quality. For MoS<sub>2</sub>/NLG, it is revealed that 30 min in Ar gas at 300° is the best condition for removing the moisture and impurities as well as for maintaining the high Raman intensity of interlayer vibrations. To understand the interfacial coupling in MoS<sub>2</sub>/*n*LG, the MoS<sub>2</sub> with layer number *m* (*m*LM) is transferred onto the *n*LG followed by annealing. Similar to other vdWHs, there are no S modes for 1LM/1LG, indicating weak interfacial coupling between the two constituents. However, in contrast to the ULF Raman spectra in tMLG, MoSe<sub>2</sub>/MoS<sub>2</sub>, MoS<sub>2</sub>/WSe<sub>2</sub> and twisted MoS<sub>2</sub>, [13, 14, 16, 17, 75] the LB modes cannot be observed in 1LM/1LG. The ULF Raman spectra of 2LM/*n*LG (*n* = 1, 2, ... 6, 8) are shown in Fig. 10.10a. The S<sub>21</sub> mode of the 2LM constituent located at the same position in all spectra, which confirms the absence of interfacial shear coupling in *m*LM/*n*LG. In addition, because the S modes of the *n*LG constituent may be overlapped by other Raman modes due to their weak intensity, they are usually not observable. Similar to the LB modes in tMLG, several LB branches can be detected in 2LM/*n*LGs, whose frequencies red-shift with increasing *n*, as indicated by the dashed lines. Because the interfacial coupling between 2LM and *n*LG is comparable to the interlayer interactions in 2LM or *n*LG, new LB modes appear as *n* increases. Considering 2LM/*n*LG as an overall system with *N* = *n* + 2,

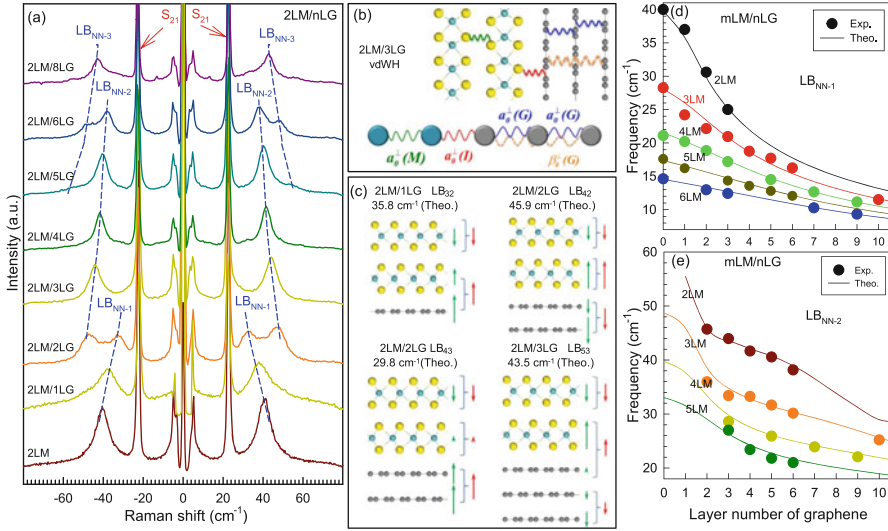


**Fig. 10.10** (a) Stokes/anti-Stokes Raman spectra of 2LM/*n*LG in the S and LB peak spectral ranges. (b) Schematic diagram of the LCM for LB modes in 2LM/3LG, in which the next nearest LB coupling in the 3LG constituent is considered. (c) Normal mode displacements of the observed LB modes in 2LM/1LG, 2LM/2LG and 2LM/3LG. The corresponding calculated (Theo.) frequencies are indicated. (d) Pos(LB<sub>NN-1</sub>) and Pos(LB<sub>NN-2</sub>) in *m*LM/*n*LG as a function of *n*. The solid lines show the theoretical trends of Pos(LB<sub>NN-1</sub>) and Pos(LB<sub>NN-2</sub>) on *n* based on the LCM. (Reproduced with permission from Ref. [20])

the LB modes can be reproduced by the LCM with the nearest LB force constant in 2LM of  $\alpha_0^\perp(M) = 84 \times 10^{18} \text{ N/m}^3$  and that in *n*LG of  $\alpha_0^\perp(G) = 106.5 \times 10^{18} \text{ N/m}^3$  and  $\beta_0^\perp(G) = 9.5 \times 10^{18} \text{ N/m}^3$  (Fig. 10.10b). The interfacial LB force constant between 2LM and *n*LG constituents is referred to as a constant  $\alpha_0^\perp(I)$  in 2LM/*n*LG, and the total layer number *N* is *n*+2. In this case, three branches of LB<sub>NN-1</sub>, LB<sub>NN-2</sub> and LB<sub>NN-3</sub> can be observed in Fig. 10.10a. Based on the experimental frequencies,  $\alpha_0^\perp(I)$  is estimated as  $60 \times 10^{18} \text{ N/m}^3$ , smaller than  $\alpha_0^\perp(M)$  but larger than  $\alpha_0^\perp(G)/2$ . According to the LCM, the corresponding normal displacements of each layer can also be obtained for each LB mode, and those of the LB<sub>NN-1</sub> mode in 2LM/1LG and 2LM/2LG as well as of LB<sub>NN-2</sub> in 2LM/2LG and 2LM/3LG are shown in Fig. 10.10c. Because the unit mass of 1LG is approximately 1/4 of that in 2LM, the 1LG are treated as a perturbation to the 2LM in 2LM/1LG. Thus, 1LG exhibits atomic displacements similar to those of its nearest MoS<sub>2</sub> layer for the LB<sub>32</sub> mode. In addition, similar behaviour can be found in *m*LM/1LG [20]. With *n* of *n*LG increasing, the *n*LG cannot be regarded as the perturbations to the 2LM for the normal mode displacements of the LB mode. However, for LB<sub>42</sub> and LB<sub>43</sub>, the top two graphene layers can be treated as a unit and thus these two modes exhibit atomic displacements similar to those of LB<sub>31</sub> and LB<sub>32</sub> in 3LM. With respect to the LB<sub>53</sub> in 2LM/3LG, the two top graphene layers can also be seen as a unit and vibrate



out-of-phase with the third graphene layer whose atomic displacements are in-phase with the nearest MoS<sub>2</sub> layer. Thus, the normal displacements of LB<sub>53</sub> are similar to those of LB<sub>31</sub> in 3LM. Therefore, the analysis of atomic displacements for each LB mode enhance the understanding of the interfacial coupling effects on the generation of new LB modes beyond those of the two constituents. Further investigations of *mLM/nLG* have been performed and the results are depicted in Fig. 10.10d, e. The LCM with  $\alpha_0^\perp(\text{I}) = 60 \times 10^{18} \text{ N/m}^3$  is enough to reproduce the frequencies of the LB<sub>*NN-1*</sub> and LB<sub>*NN-2*</sub> modes, indicating an almost uniform interlayer LB coupling in *mLM/nLG* with various twist angles. In addition, the Raman spectroscopy of *nLG/mLM* was also investigated and the LB modes were revealed to locate at peak positions almost identical to those of *mLM/nLG*, which implies that the interfacial coupling in *mLM/nLG* vdWHs is not so sensitive to the stacking order or twist angle. Similar results can also be seen in other heterostructures, such as MoSe<sub>2</sub>/MoS<sub>2</sub> [75].

## 10.5 Conclusion

In this chapter, we discussed the interlayer vibrations in 2DMs and vdWHs. The discussions starts after introducing the stacking orders and symmetries of the large family of 2DMs. Interlayer interactions play a direct role in modifying their optical and electronic properties in 2DMs and vdWHs. The ULF interlayer modes are more sensitive to vdW coupling, and their frequencies and Raman activities depend on the layer number, stacking order and symmetry. We addressed the physical origins of interlayer vibrations and then described the direct methods to probe the fundamental S and LB modes. Finally, several examples of the ULF Raman spectroscopy in various 2DMs were reviewed. The frequencies of interlayer vibrations can be defined as a rigorous function of the layer number, whereas the stacking orders and anisotropies play an important role in their Raman activities. In particular, the interlayer vibrations in twisted 2DMs or vdWHs exhibit different behaviours, which can potentially be utilized to distinguish the interfacial coupling and therefore to obtain a good understanding of these systems and their attractive applications.

**Acknowledgements** We acknowledge support from the National Key Research and Development Program of China (Grant No. 2016YFA0301204), the National Natural Science Foundation of China (Grant No. 11474277, 11874350 and 11434010), and the Beijing Municipal Science and Technology Commission.

## References

1. K.S. Novoselov, D. Jiang, F. Schedin, T.J. Booth, V.V. Khotkevich, S.V. Morozov, A.K. Geim, Proc. Natl. Acad. Sci. USA **102**(30), 10451 (2005)
2. X. Zhang, Q.H. Tan, J.B. Wu, W. Shi, P.H. Tan, Nanoscale **8**, 6435 (2016)

3. A.K. Geim, K.S. Novoselov, *Nat. Mater.* **6**(183), 183 (2007)
4. Q.H. Wang, K. Kalantar-Zadeh, A. Kis, J.N. Coleman, M.S. Strano, *Nat. Nanotechnol.* **7**(11), 699 (2012)
5. A.K. Geim, I.V. Grigorieva, *Nature* **499**(7459), 419 (2013)
6. X. Zhang, X.F. Qiao, W. Shi, J.B. Wu, D.S. Jiang, P.H. Tan, *Chem. Soc. Rev.* **44**, 2757 (2015)
7. K.S. Novoselov, A. Mishchenko, A. Carvalho, A.H. Castro Neto, *Science* **353**(6298), 9439 (2016)
8. S.N. Shirodkar, U.V. Waghmare, *Phys. Rev. Lett.* **112**, 157601 (2014)
9. X.L. Li, W.P. Han, J.B. Wu, X.F. Qiao, J. Zhang, P.H. Tan, *Adv. Funct. Mater.* **27**, 1604468 (2017)
10. L. Liang, J. Zhang, B.G. Sumpter, Q. Tan, P.H. Tan, V. Meunier, *ACS Nano* **11**(12), 11777 (2017)
11. J.B. Wu, M.L. Lin, X. Cong, H.N. Liu, P.H. Tan, *Chem. Soc. Rev.* **47**, 1822 (2018)
12. V. Carozo, C.M. Almeida, E.H.M. Ferreira, L.G. Cançado, C.A. Achete, A. Jorio, *Nano Lett.* **11**(11), 4527 (2011)
13. J.B. Wu, X. Zhang, M. Ijäs, W.P. Han, X.F. Qiao, X.L. Li, D.S. Jiang, A.C. Ferrari, P.H. Tan, *Nat. Commun.* **5**, 5309 (2014)
14. J.B. Wu, Z.X. Hu, X. Zhang, W.P. Han, Y. Lu, W. Shi, X.F. Qiao, M. Ijäs, S. Milana, W. Ji, A.C. Ferrari, P.H. Tan, *ACS Nano* **9**(7), 7440 (2015)
15. K. Liu, L. Zhang, T. Cao, C. Jin, D. Qiu, Q. Zhou, A. Zettl, P. Yang, S.G. Louie, F. Wang, *Nat. Commun.* **5**, 4966 (2014)
16. A.A. Puretzky, L. Liang, X. Li, K. Xiao, B.G. Sumpter, V. Meunier, D.B. Geohegan, *ACS Nano* **10**(2), 2736 (2016)
17. S. Huang, L. Liang, X. Ling, A.A. Puretzky, D.B. Geohegan, B.G. Sumpter, J. Kong, V. Meunier, M.S. Dresselhaus, *Nano Lett.* **16**(2), 1435 (2016)
18. K.S. Novoselov, A.H.C. Neto, *Phys. Scripta* **2012**(146), 014006 (2012)
19. Y. Gong, J. Lin, X. Wang, G. JShi, S. Lei, Z. Lin, X. Zou, G. Ye, R. Vajtai, B.I. Yakobson, H. Terrones, M. Terrones, B.K. Tay, J. Lou, S.T. Pantelides, Z. Liu, W. Zhou, P.M. Ajayan, *Nat. Mater.* **13**(12), 1135 (2014)
20. H. Li, J.B. Wu, F. Ran, M.L. Lin, X.L. Liu, Y. Zhao, X. Lu, Q. Xiong, J. Zhang, W. Huang, H. Zhang, P.H. Tan, *ACS Nano* **11**, 11714 (2017)
21. P.H. Tan, W.P. Han, W.J. Zhao, Z.H. Wu, K. Chang, H. Wang, Y.F. Wang, N. Bonini, N. Marzari, N. Pugno, G. Savini, A. Lombardo, A.C. Ferrari, *Nat. Mater.* **11**, 294 (2012)
22. J.L. Feldman, *J. Phys. Chem. Solids* **42**(11), 1029 (1981)
23. M. Gatlulle, M. Fischer, A. Chevy, *Phys. Status Solidi B* **119**(1), 327 (1983)
24. R. Nicklow, N. Wakabayashi, H.G. Smith, *Phys. Rev. B* **5**, 4951 (1972)
25. B. Yang, M.D. Morris, H. Owen, *Appl. Spectrosc.* **45**(9), 1533 (1991)
26. P.J. Horoyski, M.L.W. Thewalt, *Appl. Spectrosc.* **48**(7), 843 (1994)
27. S.G. Belostotskiy, Q. Wang, V.M. Donnelly, D.J. Economou, N. Sadeghi, *Appl. Phys. Lett.* **89**(25) (2006)
28. H. Okajima, H.O. Hamaguchi, *Appl. Spectrosc.* **63**(8), 958 (2009)
29. C. Moser, F. Havermeyer, *Appl. Phys. B* **95**(3), 597 (2009)
30. S. Lebedkin, C. Blum, N. Stürzl, F. Hennrich, M.M. Kappes, *Rev. Sci. Instrum.* **82**(1), 013705 (2011)
31. A.F.H. van Gessel, E.A.D. Carbone, P.J. Bruggeman, J.J.A.M. van der Mullen, *Plasma Sources Sci. and T.* **21**(1), 015003 (2012)
32. J. Verble, T. Wietling, P. Reed, *Solid State Commun.* **11**(8), 941 (1972)
33. R.J. Nemanich, G. Lucovsky, S.A. Solin, in *Proceedings of the International Conference on Lattice Dynamics*, Paris, 1977, pp. 619–621
34. T. Sekine, T. Nakashizu, K. Toyoda, K. Uchinokura, E. Matsuura, *Solid State Commun.* **35**(4), 371 (1980)
35. S. Sugai, T. Ueda, *Phys. Rev. B* **26**, 6554 (1982)
36. P.H. Tan, D. Bougeard, G. Abstreiter, K. Brunner, *Appl. Phys. Lett.* **84**(14), 2632 (2004)

37. Y. Zhao, X. Luo, H. Li, J. Zhang, P.T. Araujo, C.K. Gan, J. Wu, H. Zhang, S.Y. Quek, M.S. Dresselhaus, Q. Xiong, *Nano Lett.* **13**(3), 1007 (2013)
38. G. Plechinger, S. Heydrich, J. Eroms, D. Weiss, C. Schller, T. Korn, *Appl. Phys. Lett.* **101**(10), 101906 (2012)
39. H. Zeng, B. Zhu, K. Liu, J. Fan, X. Cui, Q.M. Zhang, *Phys. Rev. B* **86**, 241301 (2012)
40. M. Boukhicha, M. Calandra, M.A. Measson, O. Lancry, A. Shukla, *Phys. Rev. B* **87**, 195316 (2013)
41. Y. Zhao, X. Luo, J. Zhang, J. Wu, X. Bai, M. Wang, J. Jia, H. Peng, Z. Liu, S.Y. Quek, Q. Xiong, *Phys. Rev. B* **90**, 245428 (2014)
42. C.H. Lui, Z. Ye, C. Keiser, E.B. Barros, R. He, *Appl. Phys. Lett.* **106**(4), 041904 (2015)
43. P.H. Tan, J.B. Wu, W.P. Han, W.J. Zhao, X. Zhang, H. Wang, Y.F. Wang, *Phys. Rev. B* **89**, 235404 (2014)
44. X. Zhang, W.P. Han, J.B. Wu, S. Milana, Y. Lu, Q.Q. Li, A.C. Ferrari, P.H. Tan, *Phys. Rev. B* **87**, 115413 (2013)
45. H. Zhao, J. Wu, H. Zhong, Q. Guo, X. Wang, F. Xia, L. Yang, P. Tan, H. Wang, *Nano Res.* **8**(11), 3651 (2015)
46. J.B. Wu, H. Wang, X.L. Li, H. Peng, P.H. Tan, *Carbon* **110**, 225 (2016)
47. X.F. Qiao, J.B. Wu, L. Zhou, J. Qiao, W. Shi, T. Chen, X. Zhang, J. Zhang, W. Ji, P.H. Tan, *Nanoscale* **8**, 8324 (2016)
48. M. Miscuglio, M.L. Lin, F. Di Stasio, P.H. Tan, R. Krahné, *Nano Lett.* **16**(12), 7664 (2016)
49. X.L. Liu, H.N. Liu, J.B. Wu, H.X. Wu, T. Zhang, W.Q. Zhao, P.H. Tan, *Rev. Sci. Instrum.* **88**(05), 053110 (2017)
50. M.L. Lin, F.R. Ran, X.F. Qiao, J.B. Wu, W. Shi, Z.H. Zhang, X.Z. Xu, K.H. Liu, H. Li, P.H. Tan, *Rev. Sci. Instrum.* **87**(5), 053122 (2016)
51. Z. Li, K.F. Mak, E. Cappelluti, T.F. Heinz, *Nat. Phys.* **7**(12), 944 (2011)
52. D. Xiao, G.B. Liu, W. Feng, X. Xu, W. Yao, *Phys. Rev. Lett.* **108**, 196802 (2012)
53. J. Yan, J. Xia, X. Wang, L. Liu, J.L. Kuo, B.K. Tay, S. Chen, W. Zhou, Z. Liu, Z.X. Shen, *Nano Lett.* **15**(12), 8155 (2015)
54. T. Ritschel, J. Trinckauf, K. Koepemik, B. Buchner, M.v. Zimmermann, H. Berger, Y.I. Joe, P. Abbamonte, J. Geck, *Nat. Phys.* **11**(4), 328 (2015)
55. X. Xu, W. Yao, D. Xiao, T.F. Heinz, *Nat. Phys.* **10**(5), 343 (2014)
56. X. Luo, Y. Zhao, J. Zhang, S.T. Pantelides, W. Zhou, S. Ying Quek, Q. Xiong, *Adv. Mater.* **27**, 4502 (2015)
57. J.U. Lee, K. Kim, S. Han, G.H. Ryu, Z. Lee, H. Cheong, *ACS Nano* **10**(2), 1948 (2016)
58. X. Zhang, W.P. Han, X.F. Qiao, Q.H. Tan, Y.F. Wang, J. Zhang, P.H. Tan, *Carbon* **99**, 118 (2016)
59. X. Luo, X. Lu, C. Cong, T. Yu, Q. Xiong, S. Ying Quek, *Sci. Rep.* **5**, 14565 (2015)
60. X. Lu, M.I.B. Utama, J. Lin, X. Gong, J. Zhang, Y. Zhao, S.T. Pantelides, J. Wang, Z. Dong, Z. Liu, W. Zhou, Q. Xiong, *Nano Lett.* **14**(5), 2419 (2014)
61. A.A. Puzos, L. Liang, X. Li, K. Xiao, K. Wang, M. Mahjouri-Samani, L. Basile, J.C. Idrobo, B.G. Sumpter, V. Meunier, D.B. Geohegan, *ACS Nano* **9**(6), 6333 (2015)
62. L. Li, Y. Yu, G.J. Ye, Q. Ge, X. Ou, H. Wu, D. Feng, X.H. Chen, Y. Zhang, *Nat. Nanotechnol.* **9**(5), 372 (2014)
63. F. Xia, H. Wang, D. Xiao, M. Dubey, A. Ramasubramaniam, *Nat. Photon.* **8**(12), 899 (2014)
64. J. Qiao, X. Kong, Z.X. Hu, F. Yang, W. Ji, *Nat. Commun.* **5**(4475), 4475 (2014)
65. L.D. Zhao, S.H. Lo, Y. Zhang, H. Sun, G. Tan, C. Uher, C. Wolverton, V.P. Dravid, M.G. Kanatzidis, *Nature* **508**(7496), 373 (2014)
66. X. Ling, L. Liang, S. Huang, A.A. Puzos, D.B. Geohegan, B.G. Sumpter, J. Kong, V. Meunier, M.S. Dresselhaus, *Nano Lett.* **15**(6), 4080 (2015)
67. I. Pletikosić, M.N. Ali, A.V. Fedorov, R.J. Cava, T. Valla, *Phys. Rev. Lett.* **113**, 216601 (2014)
68. M.N. Ali, J. Xiong, S. Flynn, J. Tao, Q.D. Gibson, L.M. Schoop, T. Liang, N. Hal-dolaarachchige, M. Hirschberger, N.P. Ong, R.J. Cava, *Nature* **514**(7521), 205 (2014)
69. M. Kertesz, R. Hoffmann, *J. Am. Chem. Soc.* **106**(12), 3453 (1984)
70. C. Cong, T. Yu, *Nat. Commun.* **5**, 4709 (2014)

71. T. Jiang, H. Liu, D. Huang, S. Zhang, Y. Li, X. Gong, Y.R. Shen, W.T. Liu, S. Wu, *Nat. Nanotechnol.* **9**, 825 (2014)
72. M.P. Levendorf, C.J. Kim, L. Brown, P.Y. Huang, R.W. Havener, D.A. Muller, J. Park, *Nature* **488**, 627 (2012)
73. Y. Gong, S. Lei, G. Ye, B. Li, Y. He, K. Keyshar, X. Zhang, Q. Wang, J. Lou, Z. Liu, R. Vajtai, W. Zhou, P.M. Ajayan, *Nano Lett.* **15**(9), 6135 (2015)
74. Z. Liu, L. Ma, G. Shi, W. Zhou, Y. Gong, S. Lei, X. Yang, J. Zhang, J. Yu, K.P. Hackenberg, A. Babakhani, J.C. Idrobo, R. Vajtai, R. Vajtai, P.M. Ajayan, *Nat. Nanotechnol.* **8**, 119 (2013)
75. C.H. Lui, Z. Ye, C. Ji, K.C. Chiu, C.T. Chou, T.I. Andersen, C. Means-Shively, H. Anderson, J.M. Wu, T. Kidd, Y.H. Lee, R. He, *Phys. Rev. B* **91**, 165403 (2015)
76. W.J. Yu, Y. Liu, H. Zhou, A. Yin, Z. Li, Y. Huang, X. Duan, *Nat. Nanotechnol.* **8**(12), 952 (2013)
77. M. Massicotte, P. Schmidt, F. Vialla, K.G. Schädler, A. Reserbat-Plantey, K. Watanabe, T. Taniguchi, K.J. Tielrooij, F.H.L. Koppens, *Nat. Nanotechnol.* **11**(1), 42 (2015)
78. H. Fang, C. Battaglia, C. Carraro, S. Nemsak, B. Ozdol, J.S. Kang, H.A. Bechtel, S.B. Desai, F. Kronast, A.A. Unal, G. Conti, C. Conlon, G.K. Palsson, M.C. Martin, A.M. Minor, C.S. Fadley, E. Yablonovitch, R. Maboudian, A. Javey, *Proc. Natl. Acad. Sci. USA* **111**(17), 6198 (2014)